What can we learn from observed temperature and salinity isopycnal anomalies at eddy generation sites? Application in the Tropical Atlantic Ocean

Micael Aguedjou, A Chaigneau, I Dadou, Yves Morel, C Pegliasco, C y Da-Allada, E Baloïtcha

What can we learn from observed temperature and salinity isopycnal anomalies at eddy generation sites? Application in the Tropical Atlantic Ocean

Aguedjou H. M. A.[1,2,*], A. Chaigneau[1,3,2], I. Dadou[1], Y. Morel[1], C. Pegliasco[4], C. Y. Da-Allada[2,3,5], E. Baloïtcha[2]

[1] LEGOS, University of Toulouse, CNRS, IRD, CNES, UT3, Toulouse, France

[2] CIPMA/UAC, Cotonou, Benin

[3] IRHOB, Cotonou, Benin

[4] CLS, Ramonville Saint-Agne

[5] UNSTIM, Abomey, Benin

[*] micael.aguedjou@legos.obs-mip.fr aguhabib2000@gmail.com

Key points:

- At their generation site, 50% of observed eddies have non-significant isopycnal temperature/salinity (*θ/S)* anomalies in the TAO.
- On density-coordinates, both CEs and AEs can exhibit significant positive, negative or non-significant isopycnal *θ/S* anomalies.
- We discuss the relationship between isopycnal *θ/S* and PV anomalies and how they can inform us on their generation mechanisms.

Abstract:

Based on 18 years of satellite altimetry data and temperature/salinity (θ/S) profiles from Argo floats, we analyze the isopycnal θ/S anomalies (θ'/S') within new-born eddies in the tropical Atlantic Ocean (TAO). Our results show that on density-coordinates, both anticyclonic eddies (AEs) and cyclonic eddies (CEs) can exhibit positive, negative or non-significant θ'/S'. Almost half of the sampled eddies do not have significant θ'/S' at their generation site. The other half exhibits significant positive or negative θ', up to ±0.5 °C typically. More than 70% of them have a subsurface signature. Refined analyses of the vertical structure of new-born eddies in three selected subregions show the dominance of cold (warm) subsurface AEs (CEs) likely due to isopycnal advection of large scale potential vorticity (PV) and θ. PV is a key parameter to analyze eddy generation and dynamics. Isopycnal advection, friction or diapycnal mixing can be involved in the generation of PV anomalies from which vortices can then emerge. However, it is difficult to evaluate PV at mesoscale. In this study we propose to combine θ'/S' and PV anomalies to analyze which process could be involved in its transformation in the ocean. We argue that eddies created by diapycnal mixing or isopycnal advection of water-masses are associated with PV anomalies and significant θ'/S'. In contrast, a frictional forcing also creates PV anomalies but without modifying θ/S. Even though our results remain qualitative, the proposed diagnostics can be of interest to validate realistic models and then use them to analyze the PV anomaly sources.

Keywords: mesoscale eddies; isopycnal temperature/salinity anomalies; eddy generation mechanisms; potential vorticity; tropical Atlantic Ocean.

Plain Language Summary

Mesoscale vortices are common features in the global ocean, having typical length scales of 10 to 100 km and lifespans from several weeks to several months or even years for the more energetic structures. The vorticity of these quasi-circular rotating structures emerging from large-scale currents can be formed by several physical processes: isopycnal advection of a water mass, friction (wind stress, bottom stress) or diapycnal mixing. In this study, we first analyze the vertical structure of temperature/salinity in the eddies at their generation site. Based on the analysis of satellite and in-situ data in the tropical Atlantic Ocean, we show that ~50% of the eddies do not present significant isopycnal temperature anomalies when they are generated. In contrast, the remaining ~50% of eddies present significant isopycnal temperature anomalies, but with unexpected numerous cold anticyclones and warm cyclones. We then discuss the link between the potential vorticity and isopycnal temperature anomalies, showing combinations of the previous physical processes involved have to be invoked to explain the observed eddy characteristics.

1. Introduction

The Tropical Atlantic Ocean (TAO) is a key region for the inter-hemispheric exchange of heat, salt and mass by thermohaline circulation, large-scale currents and mesoscale eddies (e.g. Thomas and Zhai, 2013; Saenko et al., 2018). In the TAO, the upper ocean circulation is mainly composed of i) equatorial limbs of the North and South Atlantic anticyclonic subtropical gyres, ii) zonal equatorial currents and iii) near-coastal current systems (Fig. 1). In the surface layer of the North and South Atlantic subtropical gyres, the salty North and South Atlantic Waters (NAW and SAW, respectively; Fig. 1a) have maximum salinities exceeding 37 in their formation region with densities of ~25.0 – 25.5 kg m^{-3} (Tsuchiya et al., 1992; Bourlès et al., 1999a; Stramma and Schott, 1999; Stramma et al., 2005a-b Kirchner et al. 2009). In contrast, in the surface layer of the equatorial Atlantic, is found the relatively warm and fresh Tropical Surface Water (TSW; Fig. 1a) with densities lower than 24.5 kg m^{-3} (e.g. Tsuchiya et al., 1992, Tomczak and Godfrey, 1994 Stramma and Schott, 1999 ; Stramma et al., 2005a-b). Fraction of NAW and SAW is advected west-equatorward by the North Equatorial Current (NEC) and the southern South Equatorial Current (sSEC), respectively (Fig. 1a). In the equatorial region this fraction subducts and spreads below the lighter TSW forming a subsurface S maximum in the upper thermocline, known as Subtropical Underwater (STUW; Fig 1b) within the density range σ_θ ~ 24.5-26.3 kg m^{-3} (Snowden and Molinari, 2003; Tsuchiya et al., 1992; Stramma and Schott, 1999; Stramma et al., 2005b). In the upper thermocline of the eastern TAO, another salinity maximum water, known as East Atlantic Water (EAW), is observed, but noticeably fresher than the STUW (Wilson et al., 1994; Bourlès et al., 1999a; Urbano et al. 2008; Kirchner et al. 2009).

Underneath the surface waters are found the North and South Atlantic Central Waters (NACW and SACW, respectively; Fig 1b). They are characterized by a linear temperature-salinity (θ-S) relationship in the density range σ_θ ~ 25.8 - 27.1 kg m^{-3} (e.g. Emery, 2003; Liu and Tanhua, 2019) and are connected at around 15°N (Sverdrup et al. 1942; Emery and Meincke, 1986; Stramma and Schott, 1999; Stramma et al., 2005b). Below the base of the pycnocline (σ_θ > 26.0 kg m^{-3}), water-masses present θ-S properties close to the Atlantic Subarctic Intermediate Water (ASIW) in the Northern TAO and Antarctic Intermediate Water (AAIW) in the Southern TAO (e.g. Emery, 2003).

Although the relatively complex large-scale circulation shown in Fig. 1 is important for the redistribution of water-masses, mesoscale eddies are also known to play a key role in the transfer and redistribution of energy, heat, salt and physical/biogeochemical properties from their generation regions to their dissipation sites (e.g. Chaigneau et al., 2011; Gaube et al., 2014; McGillicuddy 2016). They contribute to the mixing and redistribution of water-masses through several mechanisms such as eddy horizontal stirring, eddy-induced upwelling/downwelling, subduction or trapping and self-advection over long distances across the basin (e.g. McWilliams and Flierl, 1979; Herbette et al, 2004; Chelton et al., 2011), being able to connect eastern and western boundaries (e.g., Laxenaire et al., 2018).

Eddy evolutions also strongly depend on their dynamical properties, in particular their potential vorticity (PV) signature which is a key quantity to analyze the formation and dynamics of eddies. Indeed, the core of an eddy in geostrophic equilibrium is necessarily associated with a significant isopycnal PV anomaly, from which the vorticity or stratification of the eddy core can be determined (Hoskins, 1985; Morel and McWilliams 1997; Herbette et al., 2003). Since PV is also conserved for fluid particles in adiabatic and frictionless evolution, the formation of a PV anomaly (and of an eddy subsequently) is necessarily associated with either adiabatic displacement of particles in a background PV gradient, or friction or diapycnal mixing (including the diabatic transformation associated with atmospheric heat and salt fluxes). Many studies have shown how vortices can be formed by the displacement of particles in a background PV gradient. Meridional advection on the planetary beta-plane (Wang, 2005), interaction of currents with sea-mounts, islands, or continental shelves (Aristégui et al., 1994; Herbette et al, 2004) can also be interpreted as creation of PV anomalies by isopycnal advection of particles. These processes are thought to play a significant role in the formation of mesoscale eddies at least in some regions of the TAO, such as east of the North Brazil Current (NBC) retroflection (e.g. Aguedjou et al., 2019). Some recent studies have shown that non-conservative forcings could also lead to the generation of strong PV anomalies and vortices. Indeed, theoretical and numerical studies have shown that diapycnal mixing (Haynes and McIntyre, 1987; 1990; Morel and McWilliams, 2001) and frictional effects, associated with lateral viscous layers (D'Asaro, 1988; Morel and McWilliams 2001; Akuetevi and Wirth, 2015), the wind (Thomas, 2005; Morel et al, 2006; Holmes et al, 2014; Holmes and Thomas, 2016) or with the bottom boundary layer

(Benthuysen and Thomas, 2012; Gula et al, 2015; 2016; Morvan et al, 2019), are all efficient mechanisms that can modify PV, create PV anomalies and subsequently vortical structures (Morel et al, 2019; Assene et al, 2020). Finally, also note that the well-known formation of eddies by barotropic and/or baroclinic instabilities of mean currents is related to the existence of isopycnal PV gradient of opposite signs and can be interpreted as the result of the creation of opposite sign PV anomalies or dipolar vortical structures (Charney and Stern, 1962; Morel and McWilliams, 2001). The mechanisms responsible for the determination of the PV structure of the unstable mean current is thus of fundamental importance too.

If, as noted above, there now exist several studies analyzing the origin of the processes (adiabatic, frictional or diapycnal mixing) involved in the generation of PV anomalies and subsequent formation of eddies in numerical simulations, it remains to be evaluated in nature. This is important because friction and diapycnal mixing are parameterized in numerical models, so numerical results have to be taken cautiously as long as they are not confirmed by observations. However, this is very challenging since the calculation of PV and its evolution require a three-dimensional description of currents and stratification. As such, the detailed diagnostics of PV evolution done in numerical simulation are impossible to reproduce for the real ocean. However, in the present study we propose to separate mechanisms depending on their combined effects on the transformation of PV and transformation of θ/S. Indeed, it has been shown that diapycnal mixing or advection of water masses can lead to significant PV modification accompanied by isopycnal θ/S anomalies (θ'/S'), whose sign and strength can be evaluated from in-situ data. In contrast, the effect of frictional forcings is more difficult to evaluate but friction is expected to create PV anomalies too with very weak isopycnal θ'/S'. We thus argue that isopycnal θ'/S' in vortex cores, where we know there exists significant PV anomalies, can be used to analyze some mechanisms at the origin of the transformation of PV in the real ocean, and represent a first step for the validation of numerical models in this respect.

In this study, based on observations, we thus propose to combine in-situ θ/S measurements with satellite altimetry data to estimate the isopycnal temperature/salinity anomalies (θ'/S') of eddy cores at their generation sites in the TAO. In Section 2 we describe the datasets and methods used to characterize θ'/S' inside eddies. In Section 3 we first present θ/S characteristics of the large-scale water-masses over selected isopycnal levels.

Second, we show case studies of θ'/S' inside individual eddies to illustrate that θ'/S' computed from isopycnal levels can strongly differ from the ones obtained along isobaric levels. Third, we characterize the θ/S isopycnal structure of eddies in the entire TAO and focus in some particular areas of the northern TAO. These diagnostics help i) to estimate the fraction of eddies that can participate to the trapping and redistribution of heat and salt through isopycnal advection in the TAO and ii) to depict the mean isopycnal θ'/S' in surface and subsurface new-born eddies. Finally, the possibility to infer where diapycnal mixing, isopycnal advection and/or frictional effects could play a significant role in the generation of PV anomalies forming eddy cores and determining their dynamical characteristics is discussed in Section 4, as well as the coherency of this information with the known dynamical features of the TAO.

2. Data and methods

2.1 Altimetry data and eddy tracking

Mesoscale eddies are identified and tracked in the TAO from daily maps of the Salto/Duacs absolute dynamic topography (ADT) gridded product. This multimission satellite altimetry product, was optimally interpolated onto a 0.25°×0.25° longitude/latitude daily grid (Ducet et al., 2000; Le Traon et al., 1998; Duacs/AVISO+, 2018; Pujol et al., 2016) and is freely distributed by the Copernicus Marine Environment Monitoring Service (http://marine.copernicus.eu/).

Eddies were identified from January 2000 to December 2017, using the widely used algorithm developed by Chaigneau et al. (2008; 2009). An eddy is identified by its center, corresponding to a local extremum in ADT, being maximum for an anticyclonic eddy (AE) and minimum for a cyclonic eddy (CE), and its external edge which corresponds to the outermost closed ADT contour around each detected eddy center. Eddy trajectories are constructed according to their polarity (cyclonic or anticyclonic) using the algorithm developed by Pegliasco et al. (2015). Briefly, this algorithm considers as part of the same trajectory, overlapping eddies with the same polarity detected at time t and $t + 1\ day$. If several eddies overlap, a cost function is computed to determine the most similar eddy at the time $t + 1\ day$. When no overlapping eddy is found neither

at time *t + 1 day* nor *t + 2 day*, the trajectory is stopped and the eddy is considered as dissipated. This eddy tracking algorithm is also able to successfully identify eddy-merging or eddy-splitting events (16% of the long lived tracked eddies) that frequently occur in the ocean (e.g. Pegliasco et al., 2015; Laxenaire et al., 2018). As in Aguedjou et al. (2019), in order to consider only long-lived and coherent structures, we retained eddies lasting more than 30 days and having amplitudes and radii greater than 1 cm and 30 km, respectively. A total of ~7800 long-lived AEs and ~8100 long-lived CEs were detected in the TAO between 2000 and 2017. Readers interested in more detail regarding the main characteristics and seasonality of these eddies are invited to refer to Aguedjou et al. (2019).

2.2 Argo data

2.2.1. Argo data processing

The vertical/isopycnal structure of mesoscale eddies is investigated using *θ/S* profiles acquired by Argo floats in the TAO during the 2000-2017 period. These data were collected and made freely available by the Coriolis project and programs that contribute to it (http://www.coriolis.eu.org). In the TAO, a total of 144033 *θ/S* profiles, flagged as good or probably good by the Coriolis Data Center, were quality controlled following Chaigneau et al. (2011) and Pegliasco et al. (2015). First, we retained profiles for which: i) the shallowest data is not deeper than 15 m depth and the deepest acquisition is below 950 m depth, ii) at least 30 data are available between the surface and 950 m depth and iii) the depth difference between two consecutive data does not exceed a given threshold (25 m for the 0–150 m layer, 50 m for the 150–300 m layer, 75 m for the 300–500 m layer and 100 m below 500 m depth). Second, each profile was visually inspected and was systematically discarded if it presented a suspicious *θ/S* profile. The remaining 114440 profiles (Fig. 2a), representing ~80% of the original database, were then linearly interpolated every 5 m from the surface to 300 m depth, and every 10 m below. We here assumed that the shallowest values (within 0-15 m depth) were representative of the surface values. The spatial distribution of the retained Argo profiles is rather homogeneous in the TAO, except along continental shelves or around islands where Argo floats cannot reach their nominal parking depths (Fig. 2a). About 55% of these profiles were acquired in the Northern Hemisphere, due to the higher number of international cruises and

Argo float deployments in this region. The temporal distribution of valid Argo profiles in the TAO shows a linear increase from ~200 yearly profiles in 2000 to ~12000 yearly profiles after 2017 (Fig. 2b).

2.2.2. Argo data within new-born eddies

The 114440 retained *θ/S* profiles were then classified into three categories depending on whether Argo floats surfaced within AEs or CEs (detected from altimetry) or outside eddies. However, along their trajectories, TAO eddies exhibit a three-step evolution composed of growth, mature and decay phases (Pegliasco et al., 2015; Sun et al., 2018; Aguedjou et al., 2019). During the growth phase of the eddies, which extends over the first ~30% of their lifespan, their radius, amplitude, and kinetic energy strongly increase (Pegliasco et al., 2015; Sun et al., 2018; Aguedjou et al., 2019). Also during this phase, eddies traveled on average 200 km from their generation sites (See Appendix A3 and Fig. A4d). Thus, in order to investigate the isopycnal structure of new-born eddies, close to their generation sites, and infer the physical mechanisms involved in their generation, we only retained *θ/S* profiles acquired by Argo floats that surfaced within eddies located closer than 200 km from their formation sites (Fig. 2c). Around ~25% of the ~16000 long-lived eddy trajectories were sampled within 200 km from their birth sites and are thus retained for the analysis of the thermohaline structure of new-born eddies presented in Section 3.4. The spatial distribution of the Argo floats that sampled these new-born eddies is shown in Fig. 2c. Note that varying the distance between 100 km and 300 km do not change the main results and discussion drawn in this study (not shown). We thus selected 200 km, which is a good compromise between being close enough from the eddy formation sites and having a satisfactory number of eddies sampled by Argo floats.

Figure 2d shows the mean distribution of Argo floats that surfaced within new-born eddies, as a function of the normalized radial distance from eddy centers. A normalized distance equals to 1 corresponds to the equivalent eddy radius inferred from the area enclosed by the ADT contour of the eddy-edge. Within these new-born eddies, 50% (75%, respectively) of the Argo floats surfaced within a normalized distance of 2/3 (0.9) the eddy equivalent radius from the eddy center (Fig. 2d). About 20% surfaced at a normalized radial distance

higher than 1. This occurs when eddies are deformed and the profilers surface between the equivalent radii and eddy edges.

2.3 Isopycnal temperature anomalies in new-born eddies

These depth-dependent *θ/S* profiles were first projected onto density-coordinates (here density refers to potential density referenced to the sea-surface). Second, isopycnal θ' and *S'*, were inferred for each profile by removing a local climatological profile representative of the large-scale background, also computed on density-coordinates. In a similar way to Castelao et al. (2014) and Pegliasco et al. (2015), local climatological profiles ($\bar{P}$), were obtained by weighted arithmetic means of all the available profiles (P_i) acquired outside eddies, within a radius of 200 km and separated by less than ±30 days (independently of the year) from the date of the considered profile within the eddy (see Appendix A1). Selecting outside-eddy profiles collected no more than 30 days apart of the day of the year in which the eddy profile was collected, allows us to filter out unwanted *θ/S* seasonal variations.

Vortices were then further classified into three main categories, depending on whether isopycnal θ' were i) significant (positive or negative) in the surface layer, extending from the surface to the base of the pycnocline, ii) significant (positive or negative) in the subsurface layer below the base of the pycnocline, or iii) not significant neither above nor below the pycnocline (see Appendix). The corresponding eddies are then qualified as surface eddies, subsurface eddies or eddies with non-significant anomalies, respectively. Eddies having both surface and subsurface significant isopycnal θ' are considered as subsurface eddies. Note that the nature (surface or subsurface) of the eddies is often defined based on kinematic properties such as geostrophic velocity (e.g. Chaigneau et al., 2011; Pegliasco et al., 2015), vorticity (e.g. Assene et al., 2020), or Okubo-Weiss parameter (e.g. Xu et al., 2019). Here in contrast, it is the vertical position of the significant isopycnal θ' within the eddies (above or below the pycnocline, respectively) that defines their nature (surface or subsurface).

In order to determine whether θ' within eddies are significant or not, an isopycnal θ' threshold was defined in a $1°\times1°$ longitude/latitude grid at seasonal scale, from Argo profiles that surfaced outside eddies (see Appendix). Figures 3a-b show the annual mean of θ' thresholds for the surface and subsurface layers,

255 respectively. In general, a given θ' profile acquired within an eddy is significant within the surface layer when
256 the square root of its quadratic mean values (see Eq. E4 in Appendix) integrated over the surface layer is greater
257 than 0.2-0.5 °C, except for some regions such as the frontal zone separating NAW from TSW, where θ' threshold
258 reaches up to 0.8 °C (Fig. 3a). In contrast, threshold values of θ' within the subsurface layer are much lower and
259 generally less than 0.3 °C. However, around the frontal zone along which the NEC is flowing, high θ' threshold
260 values are still noticed reaching up to 0.8 °C (Fig. 3b). Note that a classification based on Student's t-tests was
261 also performed and led to similar results at a 99% confidence level. For a given density, θ' and S' are
262 proportional and of the same sign, so that isopycnal maps of θ' or S' are similar by definition. We thus
263 hereinafter only focus on θ' along isopycnal levels.

264 It is important to note that the ocean mixed layer is the site of intense ocean-atmosphere interactions that
265 impact the mixed-layer properties from diurnal to inter-annual timescales (e.g. Guemas et al., 2011; Rugg and
266 Foltz, 2016). For instance, diurnal variations of the solar heating can modify the daily mean SST by about a 0.3°-
267 0.5 °C (even greater for extreme events) in the TAO (e.g. Guemas et al., 2011; Gentemann et al., 2008;
268 Wenegrat and McPhaden, 2015). Similarly, interannual variations of ±0.5 °C are commonly observed in the
269 TAO (e.g. Carton et al., 1996; Rugg and Foltz, 2016; Foltz et al., 2019). Thus, using Argo floats' data within the
270 mixed-layer induces relatively strong positive or negative θ/S anomalies that are not directly related to eddy
271 dynamics and are difficult to interpret. Also, this high variability, can lead to a misclassification of eddies as the
272 eddy signal in the mixed layer can be more variable than below the mixed layer. Thus in this study, surface
273 eddies refer to eddies having significant θ' between the base of the mixed layer to the base of the pycnocline.

274 **3. Results**

275 **3.1 Large-scale distribution of isopycnal temperature in the TAO**

276 In order to better understand the eddy signature on θ along isopycnal surfaces, we first briefly depict the
277 large-scale water-mass θ distribution in the TAO along two isopycnal levels. As such, Fig. 4 presents the mean θ
278 on σ_θ = 25.5 kg m^{-3} and σ_θ = 27.2 kg m^{-3} levels, obtained from Argo floats that surfaced outside eddies. These
279 two particular σ_θ levels were retained because the maximum isopycnal θ' within surface/subsurface eddies are

mostly observed close to σ_θ = 25.5/27.2 kg m^{-3} (see Fig. 7). On the shallower/lighter density-level, we can observe the noticeable warmer areas located within the subtropical gyres where NAW and SAW are located (Fig. 4a,d). On σ_θ = 25.5 kg m^{-3} isopycnal, these water-masses θ ranges from 24 to 24.5 °C and 22 to 23 °C, respectively (Fig. 4a,d). The along-isopycnal θ decreases equatorward from the gyre centers. In the eastern TAO, where EAW is originated, θ decreases to ~20 °C and S is lower than 36 (see also on Fig. 4d). Along the equator a relative warm core (θ ~ 22 °C) water-mass is advected eastward by the EUC (see Fig. 1 and Fig. 4a). The θ of this water-mass slightly decreases eastward and the water-mass is also characterized by relatively high salinities (not shown but see, e.g. Hormann and Brandt, 2007; Kolodziejczyk et al., 2009; Da-Allada et al., 2017). Finally, in the eastern boundary upwelling systems (Canary and Benguela), the mean θ is lower than 18 °C on σ_θ = 25.5 kg m^{-3} due to the presence of the wind-forced coastal upwelling (Fig. 4a). The σ_θ = 25.5 kg m^{-3} isopycnal layer deepens from ~40 m in the eastern TAO to ~140 m in the western TAO at latitudes of ±20° (black lines in Fig. 4a). The westward deepening of this isopycnal layer, which is associated with the lower part of the thermocline/pycnocline, is reduced along the equator where its depth varies from 50 m in the Gulf of Guinea to ~100 m off Brazil.

On the σ_θ =25.5 kg m^{-3} (σ_θ =27.2 kg m^{-3}, respectively) density layer, θ distribution shows a strong isopycnal θ front that separates the warmer and saltier NAW (NACW) from the colder and fresher EAW (SACW) and extends across the basin. East of ~30°W, this front is known as the Cape Verde Frontal Zone (CVFZ) (Zenk et al; 1991; Pérez-Rodriguez and Marrero-Diaz, 2001; Martínez-Marrero et al., 2008; Tiedemann et al., 2018), which is an active area of water-mass exchange associated with the formation of mesoscale eddies (e.g. Dadou et al., 1996; Schütte et al., 2016). However, we hereafter simply refer to the frontal zone to indicate the connection area between NACW and SACW. The NEC flows along this frontal zone, which is oriented southwestward from 20°N in the eastern TAO to 10°N in the western TAO (see also Fig. 1). This front is clearly visible down to σ_θ = 27.2 kg m^{-3} (Fig. 4b) where it is more diffuse and the strongest θ gradients are observed southward, between 10°N and the equator. At this density level, the frontal zone is much more zonal, and NACW and SACW have typical θ of 10-11 °C and 5-6 °C, respectively (Fig. 4b,d). The mean depth of this

isopycnal level is of ~650 m in a large part of the TAO (black lines in Fig. 4b), and deepens to 750-900 m poleward of latitudes ±20°.

Figure 4c presents the meridional θ section at 35°W. Warmer waters with θ greater than 20 °C are located above the σ_θ = 26.0 kg m^{-3} isopycnal layer and are associated with the previously described NAW, SAW and TSW. TSW is the warmest water-mass, with θ reaching 28 °C around the equator, but exhibits the lowest surface salinity of 35.5-36 (not shown) due to the excess of precipitation to evaporation in this area. Below the σ_θ = 26.0 kg m^{-3} density layer, there are the distinguishable warmer NACW and cooler SACW, separated by the θ front that becomes more diffuse below σ_θ = 27.0 kg m^{-3}.

θ/S diagrams and the main water-mass characteristics found in the TAO are depicted in Figure 4d. They were constructed from Argo floats that surfaced outside eddies within the northern, southern and eastern parts of the TAO (see boxes delimited in white in Fig 4a). This Figure confirms that TSW is much fresher and lighter than NAW or SAW and that NACW is warmer and saltier than SACW along isopycnal levels.

3.2 Case studies of iso-depth versus isopycnal temperature anomalies in mesoscale eddies

Estimates of θ and S anomalies within an eddy can strongly differ whether we use a depth-coordinate system, where the local vertical displacement of isopycnal levels strongly impacts θ'/S', or a density-coordinate system. In order to better familiarize the reader with this concept, and to help the interpretation of the results described in the following Sections, we here describe θ' observed in three individual mesoscale AEs at their generation sites, using both the depth- and density-coordinate systems. These three eddies (AE1, AE2 and AE3, respectively), detected by their ADT signature, were sampled by Argo floats in the western (AE1, Fig. 5a), central (AE2, Fig. 5b) and eastern parts (AE3, Fig. 5c) of the northern TAO. As typically observed in the TAO (Aguedjou et al., 2019), they have amplitudes of ~2-4 cm, radii of ~70-100 km, eddy kinetic energies of 85-100 cm^2 s^{-2}, and mean vorticities of 2-5×10^{-5} s^{-1}.

Although the 3 eddies were sampled by Argo floats within their core, AE1 and AE2 were sampled relatively close to their edge (Fig. 5a-b), whereas A3 was sampled in the vicinity of its center (Fig. 5c). As expected for AEs, θ' observed using a depth-coordinate system are mainly positive for the 3 case-study eddies

330 (Fig. 4d-f, magenta lines). Indeed, in depth-coordinates, the isopycnal deepening (rising, respectively) occurring
331 inside AEs (CEs), is the main driver of the observed positive (negative) θ' (e.g. Assassi et al., 2016; Keppler et
332 al., 2018).

333 The θ' computed in depth-coordinates (Fig. 5d, magenta line) suggest that AE1 is a subsurface eddy with
334 a core extending from 100 m to 600 m depth. These anomalies are in part due to the observed ~14 m deepening
335 of the subsurface isopycnal levels in AE1 (not shown). However, θ' computed in density-coordinates (but plotted
336 in Fig 5d as a function of depth by associating each isopycnal level to its depth in the analyzed profile), are also
337 significantly positive in the σ_θ ~ 25.0 – 27.4 kg m^{-3} isopycnal layer located between 100 and 800 m depth, with
338 the maximum of ~1 °C reached slightly below σ_θ = 27.0 (Fig. 5d, red line). These positive isopycnal θ' suggest
339 that diapycnal mixing or isopycnal advection from remote regions occurred during the formation of AE1. Fig. 5g
340 compares the θ/S diagrams for the Argo profile acquired inside the vortex (red) and the corresponding
341 climatological profile obtained from profiles outside eddies (green). It can be misleading since there exists
342 strong discrepancies between both profiles in low density ranges (σ_θ = 24.0-25.5 kg m^{-3}) (Fig. 5d). However,
343 given the curvatures of isopycnal lines and of the vertical profiles, the strongest isopycnal eddy θ/S anomalies
344 are obtained in the subsurface layer containing NACW. Thus, for this particular AE1 case-study, θ' are located in
345 subsurface and of the same sign (positive) for both coordinate systems.

346 In AE2, θ' computed in depth-coordinates are positive between the surface and 250 m depth, and slightly
347 negative below 250 m (magenta line in Fig. 5e). The maximum anomaly is of ~1.5 °C at ~150 m depth, thus
348 AE2 is likely a surface eddy. In A2, these positive anomalies are associated with a deepening of the near-surface
349 isopycnal levels by ~45 m (not shown). However, when computing θ' in density-coordinates, AE2 is
350 characterized by negative θ' in the surface layers reaching maximum negative anomalies of -1.5 °C for σ_θ ~ 26.0
351 kg m^{-3} at ~170 m depth (red line in Fig. 5e). Again, these strong negative isopycnal θ' suggest that AE2 contains
352 water from a remote region having distinct θ-S characteristics, or that diapycnal mixing, likely associated with
353 air-sea fluxes, locally modified the thermohaline structure of the water column. AE2 clearly illustrates the
354 differences that can exist when using depth- versus density-coordinates to compute θ/S anomalies.

Finally, in AE3, significant positive θ' computed from depth-coordinates are observed from the surface to 200 m depth (Fig 5f) with maximum anomalies of ~3.5 °C observed at ~50 m depth. However, isopycnal θ' show that this eddy does not contain significant water-mass anomalies relative to the background large-scale environment (Fig. 5f). Thus, θ' observed in depth-coordinates only result from the local deepening of ~12 m observed for the near-surface isopycnal layers (not shown). The isopycnal θ-S structure within AE3 is similar to the one usually observed in this region, with EAW and SACW in the surface and subsurface layers, respectively (Fig. 5i).

To summarize, based on 3 case-study AEs, we have shown that isopycnal θ' anomalies can strongly differ from anomalies computed from the more commonly used depth-coordinate system. Obviously, similar conclusions hold for CEs that generally depict negative anomalies in depth-coordinate system, but that can show positive, negative or non-significant anomalies in density-coordinate system. These discrepancies are problematic, in particular for the estimates of anomalous heat or salt eddy contents, and their associated transports, which are commonly computed in depth-coordinates instead of using density-coordinates.

3.3 Spatial distribution of isopycnal temperature anomalies in TAO new-born eddies

Figure 6 shows the spatial distribution of surface and subsurface eddies, as well as eddies with non-significant anomalies at their generation sites in the TAO. These sampled new-born eddies have a mean amplitude, radius and lifespan of ~ 3 cm, ~ 90 km, and 150 days respectively. These mean values are associated with standard errors of ~ 0.2 cm, ~ 2 km and ~ 7 days, respectively. A first striking result is that about half of the analyzed new-born AEs and CEs have a weak and non-significant isopycnal θ' relatively to their local environment at their generation site, with their mean θ' ranging mostly between ±0.1 °C. They cover all areas and their spatial distribution is quite identical for AEs and CEs (Fig. 6e-f). Although not associated with significant isopycnal θ', these eddies are associated with an average vertical displacement of ±10 m of their isopycnal levels, similar to those observed in eddies with significant anomalies, which shows that both type of vortices are associated with dynamical signature of similar strength. Likewise, Chen et al., (2021) reported that eddies induce an average vertical displacement of the pycnocline of the same order of magnitude in tropical

regions. As a result of the pycnocline vertical displacement, more than 90% of the new-born eddies that do not have significant isopycnal θ' anomalies, exhibit significant θ' in depth coordinates.

Thus, about half of the new-born eddies have significant θ' anomalies at their generation sites (Fig. 6a-d). Around 25% of these eddies are surface eddies whereas the remaining (~75%) exhibit significant subsurface θ'. Note however, that ~30% of these subsurface eddies also exhibit significant surface anomalies. The spatial distribution of AEs and CEs having significant isopycnal θ' is almost similar in surface and subsurface layers (Fig. 6a-b and 6c-d). In the Southern Hemisphere, eddies with significant θ' are very few and their maximum isopycnal θ' (±0.3 °C) are observed around the Benguela upwelling system. In contrast, in the Northern Hemisphere, positive and negative θ' are more similarly distributed with magnitude reaching up to ±0.8 °C along the frontal zone (Fig. 6a-b). Within the subsurface layer, AEs and CEs in the Northern Hemisphere are mostly characterized by negative and positive θ', respectively, contrary to what is observed in the Southern Hemisphere (Fig. 6c-d). Again, this observed dominance of relatively cold AEs and warm CEs in subsurface is unusual when working in depth-coordinates where the sign of the anomalies is largely driven by the deepening/rising of isopycnal layers (see Section 3.2).

As described in Section 1, different mechanisms can create PV anomalies and generate eddies. However, depending on the involved mechanisms, the newly formed eddies either have isopycnal θ'/S' or not. Frictional mechanisms such as wind, lateral friction, or current shear, produce PV anomalies without creating isopycnal θ'/S'. In contrast, the formation of PV anomalies by advection of water-masses with different characteristics or by diapycnal mixing is associated with isopycnal θ'/S'. Thus, from the results obtained above, we can conclude that about 50% of the TAO eddies are likely formed by frictional mechanisms, whereas 50% are likely formed by diapycnal mixing or lateral advection of distinct water-masses. The majority of these new-born eddies have distinct θ'/S' in subsurface isopycnal layers with cold anomalies in AEs and warm anomalies for CEs in the Northern TAO. We decided to further study this area in the following section.

3.4 Eddy isopycnal structures in selected northern TAO regions

Three sub-regions (R1 to R3, see Fig. 3-6) were defined according to their large-scale dynamics and characteristics (Fig. 1, Fig. 3 and Fig. 4a-b). R1 extends along the frontal zone separating NACW from SACW (Fig. 3). The westward NEC which flows along the frontal zone is mainly fed by the eastern branch of the North Atlantic subtropical gyre but also by the northern branch of the Guinean Dome (Fig. 1). Further west, a part of the NEC retroflects cyclonically and feeds both the eastward North Equatorial Counter Current (NECC) and the eastward North Equatorial Undercurrent (NEUC) (Fig. 1a-b; e.g. Stramma and Schott, 1999; Bourlès et al. 1999a; Schott et al., 2004). The large-scale isopycnal θ distribution (Fig. 4) shows that the NEC flows along the frontal zone that separates relatively warm and salty waters of the North Atlantic subtropical gyre from cooler and fresher waters of the equatorial Atlantic Ocean (Fig. 4). This frontal zone is known to exhibit strong meanderings and eddy generations (e.g. Dadou et al., 1996; Shütte et al., 2016; Aguedjou et al., 2019). In R2, that extends from north-east Brazil to West Africa between 0°N and 10°N (Fig. 6), is found the zonal equatorial dynamics (Fig. 1). In this region, strong instabilities are frequently observed, in particular due to the horizontal shear between the nSEC and NECC (Fig. 1) (e.g. Weisberg and Weingartner, 1988; Kelly et al., 1995; Athié and Marin, 2008; Von Schuckmann et al., 2008, Aguedjou et al., 2019). Finally, subregion R3 includes the NBC retroflection (Fig. 1a-b), and is populated by relatively large and energetic eddies whose surface properties (size, amplitude, eddy kinetic energy) exhibit a strong seasonal variability (e.g. Aguedjou et al., 2019).

Figure 7 shows for these 3 subregions the mean vertical θ' profiles inside new-born AEs and CEs using density-coordinates. As already discussed, the 3 sub-regions show a high number of non-significant anomaly profiles representing 40- 60% of observed eddies (Fig. 7, in black).

In R1, ~75% of the new-born eddies (AEs and CEs) having a significant θ' are subsurface eddies (Fig. 7a,d). Surface AEs (solid lines in Fig. 7a) and CEs (solid lines in Fig. 7d) are characterized by average θ' of ±0.5-0.7 °C between σ_θ ~ 25.5 and 26.0 kg m^{-3}. Subsurface AEs (dotted lines in Fig. 7a) and CEs (dotted lines in Fig. 7d) show maximum anomalies of ±0.4 °C between σ_θ ~ 27 kg m^{-3} and σ_θ ~ 27.2 kg m^{-3} except subsurface cold CEs whose mean anomaly of -0.5 °C is found between σ_θ ~ 26-26.5 kg m^{-3}. Interestingly, around 73% (65%, respectively) of these subsurface eddies are cold (warm) for AEs (CEs).

In R2, the surface eddies have strong anomalies of ±0.5 °C just below the mixed layer, with the maximum located in the density range of the eastward NECC and the westward nSEC, which carry relatively warm and cold water, respectively (Fig. 1a and Fig. 4a). In the subsurface layer, similarly to what is observed in R1 with a lower contrast with the surface layer, ~65% of the CEs and ~70% of the AEs that present a significant θ' are of subsurface (Fig. 7b,e). Around 82% (65%, respectively) of the subsurface sampled AEs (CEs) have cold (warm) anomalies and their maximum anomalies of ~ ±0.3 °C are located at σ_θ ~ 27.2 kg m^{-3} (Fig. 7b,e).

In R3 (Fig. 7c,f), unlike in the two previous areas, very few new-born eddies were sampled by Argo floats. Moreover ~55% of the AEs and ~65% of the CEs sampled at their generation sites do not exhibit significant θ'. The remaining sampled new-born eddies are characterized by relatively large anomalies, reaching ±1 °C for CEs and ~ ±0.7 °C for AEs. Note, that the relatively small number of sampled eddies is due both to the very few number of Argo floats in R3 and to the reduced size of this area. AEs characterized by positive θ' (red lines in Fig. 7c) show anomalies of ~0.5 °C, observed at σ_θ = 26 kg m^{-3} for surface AEs, and σ_θ = 26.8 kg m^{-3} for subsurface AEs. Surface CEs predominantly show strong positive and negative anomalies that are maximum at σ_θ = 25.5 kg m^{-3} (solid lines in Fig 7). In contrast, subsurface CEs mainly show positive θ' of 0.5 °C at the base of the pycnocline or at σ_θ ~ 27 kg m^{-3} (dotted lines in Fig. 7f). Note that the 3 profiles classified as cold subsurface CEs (blue dotted line in Fig. 7e) are characterized by strong positive anomalies between σ_θ = 24.5 kg m^{-3} and σ_θ = 26.7 kg m^{-3} and weak negative anomalies in deeper levels. Integrated in the water column, these deeper negative anomalies, that occupy a thicker layer, prevail and lead to a negative heat content anomaly that explains the classification of these profiles as cold subsurface CEs. In R3, the sampled new-born eddies were mainly formed on the eastern flank of the NBC retroflection (not shown), where relatively strong θ gradients exist. In the subsurface layer, isopycnal mixing of NACW and SACW takes place (eg. Kirchner et al., 2009).

4. Qualitative analysis and discussion

4.1 Eddy vertical structure and potential implications for heat and salt transports

The first striking result of our analysis, underlined in Fig. 6, is that about half of the analyzed eddies have non-significant isopycnal θ'/S' at their generation site. The other half is highly dominated by subsurface

eddies, with the strongest anomalies within the frontal zone in the Northern Hemisphere. The high number of subsurface eddies obtained in our study have been also previously reported in different areas of the TAO, from both numerical simulations and in-situ data. For instance, in the Canary and Benguela upwelling systems, Pegliasco et al. (2015) estimated that subsurface eddies represent between 40 and 60% of the total number of eddies. Although their analysis was based on depth-coordinates and did not specifically focused on new-born eddies, these authors also showed that 40-60% of the sampled eddies do not have statistically significant θ'/S', in agreement with our results. Other studies also revealed the presence and persistence of subsurface structures in various parts of the TAO, in the eastern and western boundary currents regions and in the subtropical gyres (e.g. Schütte et al., 2016; Garraffo et al., 2003; Assene et al., 2020; Amores et al., 2017; Laxenaire et al., 2020). However, as already discussed by Pegliasco et al. (2015), the high number of subsurface eddies could be influenced by a slight sampling bias in Argo data. Indeed, Argo floats drift for 10 days at a nominal parking depth of 500-1000 m and may therefore be preferentially trapped within subsurface eddies that reach these depths.

In terms of tracer transport, our results would suggest that only half of the analyzed eddies (eddies with significant anomalies) might potentially contribute to the heat and salt transport within the basin. However, the efficiency of the eddies to redistribute heat and salt through isopycnal advection from their formation region strongly depends on the ambient θ/S characteristics at their dissipation sites and whether or not the trapped and transported water-masses exhibit similar properties than the ambient ones. In the same way, other significant processes such as diapycnal mixing along eddy trajectories, local eddy-stirring transport associated with the lateral advection of large-scale thermohaline gradients (e.g. Sun et al., 2019) were not considered in our estimation. Making a precise quantification of the eddy heat/salt transport exceeds the scope of this study. However, it is important to recall that θ'/S' computed in depth-coordinates are largely influenced by the vertical displacement of isopycnal layers and do not reflect the net effect of eddy heat and salt contents that participate to the redistribution of heat and salt in the global ocean. As such, isopycnal coordinates must be considered when evaluating heat/salt transport by eddies.

4.2 Effect of isopycnal advection, friction and diapycnal mixing on the generation of PV anomalies

The equation of conservation of momentum and density can be written as

$$\frac{d}{dt}\vec{U}+\vec{f}\times\vec{U}=\frac{-\vec{\nabla}P}{\rho_o}-\vec{g}\frac{\rho}{\rho_o}+\vec{F} \quad (1)$$

$$\nabla(\vec{U})=0 \quad (2)$$

$$\frac{d}{dt}\rho=\dot{\rho} \quad (3)$$

where $\vec{U}=(u,v,w)$ is the velocity field, $\vec{f}$ is the Earth rotation vector, whose projection on the local vertical axis defines the Coriolis parameter *f*, P is the pressure, ρ the density of seawater and ρ_o a mean density, $\vec{g}$ is the gravity, $\frac{d}{dt}.=\partial_t.+u\,\partial_x.+v\,\partial_y.+w\,\partial_z.$ is the Lagrangian derivative. Finally $\vec{F}$ and $\dot{\rho}$ are non-conservative terms respectively representing frictional effects (acting on momentum) and diapycnal mixing (acting on θ and/or S and finally modifying the particle potential density). As shown by Ertel (1942; see also Muller, 2006; Morel et al, 2019; Assene et al, 2020), we can define a generalized PV as:

$$PV=-(\vec{\nabla}\times\vec{U}+\vec{f}).\vec{\nabla}Z(\rho) \quad (4)$$

The traditional Ertel PV (obtained with Z(ρ) = ρ) is dominated by the signature of the pycnocline, so that the dynamical signal associated with isopycnal variations of PV is difficult to identify. In the following, we will use the rescaled PV, as proposed in Delpech et al (2020) and Assene et al (2020), determined by choosing Z(ρ*) = z for a specific location, where the density profile ρ*(z) is typical of the stratification of the area. The rescaled PV is close to the quasi-geostrophic PV and scales as a vorticity with a reference PV value at rest close to *f*. Its evolution equation is (see Muller, 2006):

$$\frac{\partial PV}{\partial t}=-\vec{\nabla}.(\vec{U}.PV+\vec{F}.\vec{\nabla}Z(\rho)+(\vec{\nabla}\times\vec{U}+\vec{f}).\dot{Z}(\rho)) \quad (5)$$

This equation shows that PV anomalies can be formed by adiabatic displacement of water parcels in a background PV gradient, frictional effects (associated with the forcing term $\vec{F}$) and diapycnal mixing

(associated with the forcing terms $\dot{\rho}$ and $\dot{Z}(\rho)=\partial_\rho Z(\rho)\dot{\rho}$). We assume the modification of PV and θ takes place in water masses of larger scale currents, and that vortices emerging from these currents keep similar characteristics. Figure 8 qualitatively describes the expected effects of the identified three main mechanisms on both the formation of PV and θ anomalies. First, since a water mass has specific isopycnal θ (and S) but generally also PV signatures, the adiabatic displacement of a water mass to a region with different characteristics potentially leads to the generation of eddies whose cores contain both PV and θ anomalies (Fig. 8 a-b). Second, if both diapycnal fluxes $\dot{\rho}$ and frictional effects $\overrightarrow{F}$ can generate significant PV anomalies and potentially strong eddies (Fig. 8c,e) (see Morel et al, 2019 and references therein), only diapycnal fluxes (induced by mixing or atmospheric fluxes) are also associated with a modification of the θ/S properties and the generation of isopycnal θ anomalies (Fig. 8c-d). It is interesting to notice that interior mixing (Fig. 8c-d) generates new isopycnal characteristics (green patch in Fig. 8d) that necessarily remain in the convex envelope of the initial background θ/S profile (light green area, see Penney et al., 2020), whereas atmospheric fluxes can substantially alter the initial θ/S properties of waters (red characteristics). In contrast, the frictional term acts on momentum and thus on PV (Fig. 8e), but does not affect other tracers, so that no isopycnal θ anomalies are expected (Fig. 8f). To conclude, among the mechanisms that can lead to the formation of PV anomalies and eddies, friction is the only one which does not create isopycnal θ anomalies.

If a rigorous evaluation of the PV production rate requires 3D fields, as explained in Assene et al (2020), we can simplify Eq. (5) to estimate order of magnitudes for some terms. First, in a background PV gradient β_{bg}, isopycnal advection of water parcel will generate a PV anomaly

$$\delta\mathrm{PV} = \beta_{bg}\delta Y \qquad (6)$$

where δY represents the displacement of the fluid parcels along the PV gradient. Similarly, for this adiabatic process, an isopycnal temperature anomaly is created with

$$\delta\theta = \gamma_{bg}\delta Y \qquad (7)$$

where γ_{bg} is the background temperature gradient (assumed to be in the same direction as the PV gradient for simplicity).

The effect of diapycnal mixing on PV is controlled by the impermeability theorem (Haynes and McIntyre, 1987). This powerful principle allows to evaluate the modification of PV within a layer subject to diapycnal fluxes. We get (see and McIntyre, 1987; Morel and McWilliams, 2001)

$$\delta PV = -f\frac{\delta V}{V} \qquad (8)$$

where V is the initial volume of the region undergoing mixing and δV is its variation associated with mixing. In contrast, the evolution temperature, in a layer subject to mixing, depends on values of temperature in adjacent layers. It can be roughly estimated considering a volume V of water in a layer, having an initial temperature θ_i mixes with a volume δV of an adjacent layer having a temperature θ_a. The modification of temperature in the initial layer is then:

$$\delta\theta = \frac{\delta V}{V+\delta V}\left(\theta_a - \theta_i\right) \qquad (9)$$

Finally, the effect of friction is more complicated to evaluate, as it depends on details of the wind or bottom stress structure and stratification close to the boundary but it is known to yield important PV changes too (see Thomas, 2005; Morel et al, 2006; Benthuysen and Thomas, 2012; Gula et al, 20015, 2016), but the frictional forcing term does not modify temperature or salinity.

In order to analyze the effect of these processes, we computed a mean large-scale rescaled PV, calculated using Eq. (4), where $\vec{U}$ is the geostrophic velocity field computed from the World Ocean Atlas *θ/S* climatology (Locarnini et al., 2018; Zweng et al., 2018) with a level of no motion at 1000 m depth and where the reference profile to define Z(ρ) is chosen at 27°W, 7.5°N, a dynamically less intense area corresponding also to a lower surface density. Figure 9a,c show the spatial distribution of the obtained rescaled PV, averaged within both a near-surface (σ_θ =25.75 - 26.5 kg m^{-3}) and a subsurface layer (σ_θ =26.9 - 27.4 kg m^{-3}). For each layer, the mean θ distribution is also shown by black contours (Fig. 9a,c).

In R1, a reservoir of relatively strong (weak, respectively) positive PV, associated with relatively cold (warm) water is observed on the southern (northern) edge of the thermal front in the surface layer (Fig. 9a). Thus in this layer, an isopycnal PV advection tends to generate either i) positive PV anomalies associated with negative θ',

leading to the formation of cold core surface CEs, or ii) negative PV anomalies associated with positive θ', leading to the generation of warm-core surface AEs. This PV/θ relationship is better depicted in Fig. 9b. In contrast, in R2, maximum positive PV are associated with warmer θ, suggesting that isopycnal advection tends to generate cold AEs and warm CEs in the surface layer of this region (Fig. 9a-b). In R3, as shown in Fig. 9b, the PV/θ relationship is more complex and not strictly monotonic, suggesting that both warm and cold CEs and AEs can be generated by isopycnal advection, although the general tendency is closer to the R2 region (cold AEs and warm CEs). From Figure 7, we indeed observed a higher number of cold AEs in the surface layer in R2 and R3, representing ~ 66% of the significant surface eddies.

In R1, the background gradient of PV is $\beta_{bg} \sim 2\times10^{-11}$ m^{-1} s^{-1}, similar to the planetary beta (but note the gradient has opposite orientation here). The background gradient of temperature has the same direction and we can estimate $\gamma_{bg} \sim 4\times10^{-6}$ °C m^{-1}. From Eq. (6) and (7) we can thus estimate that to create an eddy with significant vorticity and PV anomaly, say $\delta PV \sim \pm10^{-5}$ s^{-1}, by isopycnal advection, fluid parcels must be displaced by $\delta Y \sim$ 500 km. This yields a temperature anomaly $\delta\theta \sim \pm2$ °C (positive for AEs and negative for CEs) which is 3 to 4 times the commonly observed anomalies in the area for these types of vortices. Thus, even for vortices whose PV and temperature anomalies are coherent with the background fields and could possibly be generated by isopycnal advection, other processes probably play a role in their generation. Evaluating the possible influence of diapycnal mixing of the near surface layer with the deeper subsurface one, Eq. (8) shows that a relative increase of volume $\delta V/V \sim 0.25$ is necessary to reach $\delta PV \sim 1.\ 10^{-5}$ s^{-1} (using f ~ 4. 10^{-5} s^{-1}). Taking a temperature difference of $\theta_i - \theta_a \sim 5$ °C between adjacent layers, we get $\delta\theta \sim 1$ °C, about 2 times the observed anomalies in the area, so atmospheric fluxes, or other processes, also probably have to be taken into account if diapycnal mixing is to explain the characteristics of observed eddy structures. As mentioned above it is difficult to evaluate the effect of a frictional term, but this mechanism creates PV anomalies without modifications of the isopycnal temperature, so it cannot explain alone the formation of eddies with significant temperature anomalies. We can conclude that in region R1, in the near surface layer, the PV and temperature structure of most eddies are probably determined by a combination of processes to explain the observed limited temperature anomalies while still leading to significant PV anomaly, and vorticity.

PV/θ relationships were also examined in the subsurface layer where we note a general northward increase of both the PV and θ (Fig. 9c). This distribution, as well as the main PV/θ relationship shown in Fig. 9d, suggests that large-scale isopycnal advection leads to the formation of cold subsurface AEs and warm subsurface CEs in the TAO. Thus, isopycnal advection likely explains the dominance (65-80% of the subsurface structures) of warm CEs and cold AEs observed from the Argo profiles in R1 and R2 (Fig. 7). For other eddies, similar analysis as proposed above can be performed and yield the same conclusions: a combination of processes is necessary to explain some of the observed eddy structures.

Note that the PV (and temperature) structure of eddies without significant isopycnal θ'/S' signature could be explained by frictional effects alone. Since they are present everywhere and represent about half the eddy population, this would suggest that wind and bottom stress are important mechanisms in the transformation of PV and creation of PV anomalies feeding the core of eddies in the TAO. Likewise, it is tempting to argue that friction could also explain the generation of PV anomalies for vortices exhibiting significant but unstructured θ'/S' signature. Note that even a constant wind (with weak Ekman pumping effects) is able to modify PV along a front (Thomas, 2005), a process that also leads to the destabilization of upwelling currents (Morel et al., 2006), strong modification of Ekman drift (Morel and Thomas, 2009) or the reinforcement of preexisting vortical structures (Holmes et al., 2014). However, this remains hypothetical, and specific combinations of advection and mixing can also be imagined to explain the observed structures. In fact, up to now, we did not find a way to evaluate the influence of friction in the transformation of PV from observations alone.

4.3 Limitations of the study

Diagnostics proposed in this study remain mostly qualitative, but, to our knowledge, it is the first attempt to analyze the importance of non-conservative effects in the generation of eddies and their associated θ/S and PV properties using only observations. The respective influence of the wind-stress and diapycnal mixing in the formation of vortices can serve as reference for realistic numerical models, for which these processes are parameterized. Given the reasonable number of eddies sampled in this study, the statistics calculated here are

599 thought to be significant, but could obviously be refined in the future, when more observations become
600 available.

601 Although our classification of significant versus non-significant θ'/S' is robust, it is important to point
602 out some limitations of our diagnostics. First, the fact that eddies must be sampled at their generation (±200 km)
603 sites strongly reduces the number of analyzed eddies.

604 Second, some of Argo profiles classified as outside eddy profiles might have sampled vortices which
605 were not detectable by altimetry, as it has been highlighted by previous studies (e.g. Garraffo et 2003; Assene et
606 al., 2020). The isopycnal θ climatology, obtained from profiles supposedly acquired outside eddies and used to
607 evaluate eddy anomalies could be slightly spoiled by this effect. However, given the very large number of Argo
608 profiles available, we believe this remains marginal.

609 Third, the exact location, relative to the eddy-centers, of Argo floats that surfaced within eddies were not
610 considered when calculating the eddy θ'/S' (Fig. 2d). However, both theoretically and practically, Argo vertical
611 profiles are on average acquired at a distance of 2/3 of the equivalent eddy radius from the eddy center (e.g.
612 Chaigneau and Pizarro, 2005; Pegliasco et al., 2015; Fig 2d). Although it may slightly impact our results, eddy
613 cores can generally be considered as homogeneous in θ/S and the general discussion on the mechanisms
614 involved in the generation of θ'/S', that shape the whole eddy structure from the eddy center to the eddy edge,
615 remains valid.

616 Fourth, in Fig. 8 we assumed the PV and θ characteristics of eddies are determined by the properties of
617 the water-mass forming their cores, so the generation process itself is adiabatic (such as baroclinic/barotropic
618 instabilities, overshoot of a current at a cape, …). Friction or mixing could act during the formation process, and
619 we can even imagine that they directly create eddies. This is the case for the formation of eddies by local wind or
620 bottom stress in the lee of islands (e.g. Pullen et al, 2008; Ioannou et al, 2020) or local convection (McWilliams,
621 1985). However, we think these events do not modify our interpretation as even at local scales advection,
622 friction or mixing have the same qualitative effects on PV and θ'/S'. One may also wonder how the complex
623 eddy dynamics, characterized by frequently observed merging or splitting events, may influence our results. In

our study, which focused on the eddy isopycnal structure close to the eddy generation sites, only splitting events can be problematic because the eddy tracking algorithm considers that a new eddy is formed at the separation site of the parent trajectory (e.g. Pegliasco et al., 2015; Laxenaire et al., 2018). However, among the ~3700 new-born eddies sampled by Argo floats in the TAO, only ~590 (16%) were associated with splitting events. Excluding these eddies from the analyses did not alter the main results and conclusions drawn in this study. However, this point could deserve special consideration in future investigations.

Fifth, although satellite altimetry has been proven to be an efficient approach to identify and track subsurface eddies (e.g. Ciani et al., 2017), the exact position of the birth location of subsurface eddies could be slightly biased using altimeter data. Indeed, subsurface eddies do not necessarily have a clear signature on sea surface height which prevents their identification in altimetry maps (e.g. Assene et al., 2020). Therefore, in our study, some subsurface eddies could have been formed a few days/weeks before being detected by altimetry. However, quantifying such biases is not possible without using three-dimensional numerical simulations (e.g. Ciani et al., 2017), what is beyond the scope of the present study.

Sixth, we argued that the effect of a frictional forcing term $\vec{F}$ (Eq. 1) on PV modification (Eq. 5) is difficult to assess. An additional difficulty is that frictional processes are generally also accompanied with diapycnal mixing. This is indeed generally the case for the wind stress, which can thus be expected to lead to modification of θ/S too. However, strong mixing is usually associated with convection generated by atmospheric heat fluxes, or strong vertical shear in ocean currents. Without such strong preconditioning, diapycnal mixing associated with the wind or bottom stress is expected to be weak, with θ'/S' remaining non-significant.

Finally, Classification of eddies with significant vs non-significant temperature anomalies relies on thresholds defined according to the local background variability and computed from Argo profiles that surfaced outside eddies (Appendix A2). This variability represents the typical anomaly a particle can get when displaced adiabatically over a typical vortex diameter. Thus a vortex whose core has an isopycnal θ' below the threshold must have gained its PV anomaly from processes that do not significantly alter the local water masses, which is typical of friction. We used the 80^{th} percentile of this variability to define θ' threshold, since the isopycnal θ' profiles are distinguishably different from those of eddies with significant θ' (see Fig. 5d-f

and 7). The number of identified eddies obviously depend on the choice of the percentile but the proportion of eddies with non-significant θ' remains important as long as the chosen percentile remains reasonable (the proportion is still 40% when choosing the 70th percentile, it reaches 70% when choosing the 90th percentile). Likewise, results are also sensitive the confidence level chosen for the performed Student's t-test. Indeed, the more we decrease the confidence level of the Student's t-test, the more we increase the number of significant anomalies.

5. Summary and perspectives

Combining 18 years of satellite altimetry and θ/S data acquired by Argo floats in the TAO, we first showed that isopycnal θ'/S' can strongly differ from the ones obtained using depth-coordinates. Indeed, although AE (CE, respectively) mostly induced positive (negative) θ'/S' in depth-coordinates, both AE and CE can exhibit positive, negative or non-significant isopycnal θ'/S'. We then focused on the vertical structure of eddies close to their generation site, to investigate the proportion and distribution of new-born eddies and found that half of the total analyzed new-born eddies in the TAO are characterized by non-significant θ'. In contrast, the second half, composed of 70% of subsurface, and of 30% of near-surface eddies, likely involve diapycnal mixing and/or lateral advection. As a consequence, in terms of tracer transport, our results would suggest that eddies that are generated with a significant θ'/S' mostly contribute to heat and salt transport in the TAO.

Refined diagnostics in three selected subregions in the northern TAO, were proposed. Along the frontal zone and in the northern equatorial subregions, the mean vertical structure of eddies is dominated by subsurface eddies with maximum anomalies reaching up to ±0.5 °C mostly found between σ_θ = 27 and 27.2 kg m^{-3} isopycnal layers. For these subsurface eddies, ~75% of AEs exhibit a negative maximum θ' whereas ~65% of CEs maximum θ' are positive. In the third subregion, within the NBC retroflection, results are questionable because of the reduced number of eddies sampled by Argo profiles at their generation sites.

We then proposed qualitative diagnostics based on the links between θ'/S' and PV anomalies under the influence of isopycnal advection, friction or diapycnal mixing. For eddies with significant anomalies, in the surface layer, PV/θ relationships suggest that isopycnal water-mass advection can explain the generation of PV

anomalies of cold core AEs observed in R2 and R3 areas. In contrast, in R1, isopycnal advection would preferentially lead to the generation of cold core CEs and warm AEs. But observations show no preference in θ'. Thus isopycnal advection alone cannot explain our diagnostics and, to modify PV or θ'/S' structures of water-masses, other processes must be involved too. Both the wind-stress or diapycnal mixing can explain the observations and, even though we think friction is probably a key process to explain the observed characteristics, it seems difficult to prove that one process is more important than the other. Additional diagnostics can be imagined to further analyze the relative influence of each process. For instance, friction associated with the wind stress is probably sensitive to the position of the ITCZ in the studied region, leading to weaker stress in summer in R1, when the ITCZ migrates from the equator to this region. Preliminary analysis has shown that the production rate of eddies with non-significant θ'/S' drastically drops during summer, which could be a sign that friction is indeed a major mechanism for the generation of PV and vortices in this region. However, this drop also exists for some other vortex types, and the atmospheric heat fluxes also vary seasonally, so the interpretation is not easy and deeper analyses are necessary before concluding. In the subsurface-layer, water-mass advection is also suggested to explain the formation of PV anomalies of warm (cold, respectively) core CEs (AEs) especially in R1 and R2, which indeed corresponds to the distribution dominantly observed.

As far as perspectives are concerned, this study provide a new diagnostics that can be useful for numerical models. As mentioned above, frictional and diapycnal mixing effects are parameterized in the models, and thus imperfectly represented. Given the qualitative link between these processes and the transformation of both PV and isopycnal θ'/S' fields, combined diagnostics involving isopycnal θ'/S' and vorticity of eddies is thus challenging for numerical results. In particular, since a major fraction of the observed eddies are associated with non-significant θ/S anomalies, frictional effects are thought to play a major role in the generation of their PV structure. Parameterizations of frictional effects are very difficult to evaluate and remain one of the Achille's heel of circulation models at mesoscale. The proposed diagnostics can thus be very useful to compare different parameterizations. Further, it would be interesting to combine isopycnal θ/S structures with trajectories to infer the long term behavior of specific long-lived eddies, having been sampled at different times by Argo floats, to analyze the evolution of their heat/salt contents. The present general approach can also be applied to other

regions to infer the relative contribution of friction and diapycnal mixing or isopycnal advection in the PV sources forming the core of eddies, using only observations, particularly in energetic areas such as the Gulf Stream and Kuroshio or in specific regions where wind-stress curl lead to the eddy generation (Canary, Ierapetra, etc.). Finally, when a significant number of Argo floats will be equipped with biogeochemical sensors (dissolved oxygen, nutrients, chlorophyll-a, …), it will be very interesting to evaluate if there exists some structuring in the transport of biogeochemical tracers by AEs and CEs, in particular in the TAO. Indeed, combining different tracers with different sources and sinks can help to more precisely identify the physical mechanisms responsible for the transformation of the water characteristics, including their PV.

Appendix A: Determination of the significance of eddy temperature anomalies

A1. Weighted arithmetic means

Isopycnal θ'/S' were computed for each Argo profile acquired within a new-born eddy by removing a local climatological profile representative of the large-scale background, also computed on density-coordinates. These local climatological profiles ($\bar{P}$) were obtained by weighted arithmetic means of all the available profiles (P_i) acquired outside eddies, within a radius of 200 km and separated by less than ±30 days (independently of the year) from the date of the considered profile. Weighted arithmetic mean profiles ($\bar{P}$) were computed by equation E1:

$$\bar{P} = \frac{1}{\sum \Omega_i(r_i, t_i)} \sum \Omega_i(r_i, t_i) \,.\, P_i(\rho) \qquad \text{(E1)}$$

where Ω_i are the weights, assigned to each profile, which depend on the distance (r_i) and time (t_i) of the profile P_i (outside eddies) from the considered profile (located inside the eddy):

$$\Omega_i(r_i, t_i) = e^{\frac{-1}{2}\left[\left(\frac{r_i}{\Delta R}\right)^2 + \left(\frac{t_i}{\Delta t}\right)^2\right]} \qquad \text{(E2)}$$

where ΔR = 100 km and Δt = 15 days are the typical length and time scales. The choice of ΔR and Δt does not significantly alters $\bar{P}$ and the results presented in the study.

A2. Temperature anomaly threshold

In order to determine whether *θ′/S′* obtained within new-born eddies are significant or not, a climatology of monthly isopycnal *θ′* thresholds was computed on a 1°×1° longitude/latitude grid within surface and subsurface layers. The surface layer extends from the base of the mixed layer to the base of the seasonal pycnocline and the subsurface layer extends from the base of the pycnocline to the deepest isopycnal level (Fig. A1). As in de Boyer Montégut et al. (2004), the mixed layer depth was defined as the depth where the density increased by 0.03 kg m $^{-3}$ from its value at 10 m depth. The reference depth was chosen at 10 m in order to avoid the strong diurnal cycle that occurs in the first few meters of the ocean (de Boyer Montégut et al. 2004). The base of the pycnocline was determined as the depth of fluid layer possessing one half of the maximum of the squared buoyancy frequency (see Cheng and Hsu, 2014). The square buoyancy is defined as :

$$N^2 = \frac{-g}{\rho}\frac{d\rho}{dz} \qquad \text{(E3)}$$

where g, ρ and z, are gravity, density, and depth, respectively.

Typically, the surface layer extends from σ_θ ~ 22 kg m^{-3} to σ_θ ~ 26 kg m^{-3} density layers in equatorial regions (15°N-15°S), and from σ_θ ~ 25 kg m^{-3} to σ_θ ~ 26.5 kg m^{-3} at mid-latitudes (15-30°). In both areas, the subsurface layer extend from the base of the surface layer to σ_θ ~ 27.5 kg m^{-3}. In both the surface and subsurface layers (Fig. A$_1$), the monthly climatological *θ′* thresholds were computed at each grid point as follows: first, we selected all the profiles within 200 km around the grid point, that surfaced outside eddies during the corresponding month (regardless of the year). Second, we computed for each profile, the square root of the quadratic mean of *θ′* integrated over the layer thickness using equation E4.

$$M_1 = \sqrt{\frac{1}{\sum h(\rho_i)} . \sum h(\rho_i) . \left(\theta'(\rho_i)\right)^2} \qquad \text{(E4)}$$

where h(ρ_i) and $\theta'(\rho_i)$ are the thickness and the θ' of the isopycnal layer ρ_i. Third, we retained the 80th percentile of M1 values as the monthly θ' threshold at the considered grid-point. This percentile was carefully chosen after a sensitivity study and is considered as significantly different from noise. For accuracy reasons, at least 30 monthly profiles are required around the grid-point to compute the threshold. Figures A2 and A3 show the monthly θ' threshold distributions for the surface and subsurface layers. Note the relatively high θ' threshold within the frontal zone throughout the year in both layers. No strong seasonality was observed, except a slight increase of the θ' threshold value in February in the surface layer (Fig. A2).

Isopycnal θ' observed in an eddy is considered as significant if its M1 values in surface and/or subsurface are higher than the corresponding thresholds shown in Fig. A2-A3. In contrast if M1 values in the eddy are lower than the corresponding thresholds in both the surface and subsurface layers, eddy anomalies are classified as non-significant. When an anomaly is significant in a given layer, its sign is given by that of the mean θ' computed over the layer, as follow:

$$M_2 = \frac{1}{\sum h(\rho_i)} . \sum h(\rho_i) . \theta'(\rho_i) \qquad \text{(E5)}$$

A similar method was used by Itoh and Yasuda (2010) to identify warm and cold eddies in the northwestern Pacific ocean.

A3. Mean eddy dynamic properties

The mean evolution of the study eddy properties (amplitude, radius and kinetic energy), similarely to what has been already observed by several observational (e.g. Pegliasco et al., 2015; Sun et al., 2018; Aguedjou et al., 2019) and numerical (Kurian et al., 2011) studies, follows three main phases during eddy life-cycle: the growth phase, the maturity phase and the dacaying phase (Fig A4a-c). The first 20-30% of eddy lifespan represents eddy growth phase during which eddy properties stongly increase, whereas the maturity phase corresponds to a plateau-like evolution of the mean properties representing 20-30% to ~ 80 % of eddy lifespan.

The decaying phase is the last phase of eddy life-cycle during which eddy properties decrease rapidely. During the growth phase, TAO eddies travel on average over 200 km (Fig A4d).

Acknowledgments:

This work was supported by the Alti-ETAO project founded by the French National Center for Space Studies (CNES) through the Ocean Surface Topography Science Team (OSTST) and supported by the French National Institute of Sciences of the Universe (INSU/CNRS). This work is also a contribution to the junior team "SAFUME" (JEAI-SAFUME) associated with the French National Research Institute for Development (IRD) and to the EU H2020 TRIATLAS project under grant agreement 817578. M. Aguedjou was supported by a PhD fellowship from the IRD and the Cultural Action and Cooperation Service (SCAC) of the French Embassy in Benin.

Gridded altimetry data were produced by SSALTO/DUACS and distributed by the Copernicus Marine Environment Monitoring Service (http://marine.copernicus.eu/) and Argo data were collected and made freely available by the Coriolis project and programs that contribute to it (http://www.coriolis.eu.org).

We sincerely thank the three anonymous reviewers for their constructive criticism and comments, which greatly improved the quality of this study.

References

Aguedjou, H. M. A., Dadou, I., Chaigneau, A., Morel, Y., & Alory, G. (2019), Eddies in the Tropical Atlantic Ocean and their seasonal variability. *Geophysical Research Letters*, 46. https://doi.org/10.1029/2019GL083925

Akuetevi, C. Q. C. & Wirth, A. (2015), Dynamics of turbulent western-boundary currents at low latitude in a shallow-water model, *Ocean Sci.*, 11, 471–481, https://doi.org/10.5194/os-11-471-2015

Amores, A., Melnichenko, O. & Maximenko, N. (2017), Coherent mesoscale eddies in the North Atlantic subtropical gyre: 3-D structure and transport with application to the salinity maximum, *Journal of Geophysical Research: Oceans*, *122*(1), 23–41, doi:10.1002/2016jc012256.

Aristégui, J., Sangra, P., Hernandez Leon, S., Canton, M., Hernandez Guerra, A., & Kerling, J. L. (1994), Island induced eddies in the Canary Islands. *Deep Sea Research Part I: Oceanographic Research Papers*, 41(10), 1509–1525. https://doi.org/10.1016/09670637 (94)90058 2

Assassi, C., Morel, Y., Vandermeirsch, F., Chaigneau, A., Pegliasco, C., Morrow, R., et al. (2016). An index to distinguish surface and subsurface intensified vortices from surface observations. *Journal of Physical Oceanography*, 46(8), 2529–2552. https://doi.org/10.1175/JPO-D-15-0122.1

Assene, F., Morel, Y., Delpech, A., Aguedjou, M., Jouanno, J., Cravatte, S., et al. (2020). From mixing to the large scale circulation: How the inverse cascade is involved in the formation of the subsurface currents in the Gulf of Guinea. Fluids, 5(3), 147. https://doi.org/10.3390/ fluids5030147

Athié, G & Marin, F. (2008), Cross-equatorial structure and temporal modulation of intraseasonal variability at the surface of the tropical Atlantic Ocean, *J. Geophys. Res*., 113, C08020, doi :1029/2007JC004332.

Benthuysen, J. & Thomas, L. (2012), Friction and Diapycnal Mixing at a Slope: Boundary Control of Potential Vorticity. *J. Phys. Oceanogr*. 42, 1509–1523.

Bourlès, B., Gouriou, Y., & Chuchla, R. (1999a), On the circulation in the upper layer of the western equatorial Atlantic. *Journal of Geophysical Research* 104, 21,151–21,170.

Carton, J., A., Cao X., Giese, B., S., & da Silva, A., M. (1996), Decadal and interannual SST variability in the tropical Atlantic Ocean. *Journal of Physical Oceanography* 26: 1165–1175.

Chaigneau, A., Eldin, G., & Dewitte, B. (2009), Eddy activity in the four major upwelling systems from satellite altimetry (1992–2007), *Prog. Oceanogr*., 83(1–4),117–123, doi:10.1016/j. Pocean.2009.07.012

Chaigneau, A., Gizolme, A., & Grados, C. (2008), Mesoscale eddies off Peru in altimeter records: Identification algorithms and eddy spatio-temporal patterns, *Prog. Oceanogr*.,79(2–4), 106–119,doi:10.1016/j.pocean. 2008.10.013.

Chaigneau, A., Le Texier A., Eldin G., Grados C., &Pizarro O. (2011), Vertical structure of mesoscale eddies in the eastern South Pacific Ocean: A composite analysis from altimetry and Argo profiling floats, *Journal of Geophysical Research, 116*(C11), doi:10.1029/2011jc007134.

Chaigneau, A., & Pizarro, O. (2005), Eddy characteristics in the eastern South Pacific, *J. Geophys. Res*., 110, C06005, doi:10.1029/2004jc002815.

Charney, J. G., & Stern, M. E. (1962), On the stability of internal baroclinic jets in a rotating atmosphere. *Journal of the Atmospheric Sciences*, 19(2), 159–172. https://doi.org/10.1175/1520 0469(1962)019<0159:OTSOIB>2.0.CO;2

Chelton, D. B., Schlax, M. G., & Samelson, R. M. (2011), Global observations of nonlinear mesoscale eddies, *Progress in Oceanography*, *91*(2), 167–216, doi:10.1016/j.pocean.2011.01.002.

Chen, X., Li, H., Cao, C. Chen, G. (2021), Eddy-induced pycnocline depth displacement over the global ocean. *Journal of Marine Systems*, *221* (2021) 103577, *https://doi.org/10.1016/j.jmarsys.2021.103577*

Cheng, M.-H., & Hsu J.R.-C. (2014), Effects of varying pycnocline thickness on interfacial wave generation and propagation, *Ocean Engineering*, *88*, 34–45, doi:10.1016/j.oceaneng.2014.05.018.

Ciani, D., Carton, X., Aguiar, A., B., Peliz, A., Bashmachnikov, I., Ienna, F., Chapron, B., &Santoleri, R. (2017), Surface signature of Mediterranean water eddies in a long-term high-resolution simulation, *Deep Sea Research Part I: Oceanographic Research Papers*, *130*, 12–29, doi:10.1016/j.dsr.2017.10.001.

Csanady, G. T. (1987), What controls the rate of equatorial warm water-mass formation? *J. Mar. Res*., 45, 513 –

532.

D'Asaro, E. A. (1988), Generation of submesoscale vortices: A new mechanism. *Journal of Geophysical Research: Oceans*, 93 (C6), 6685-6693.

Da-Allada, Y. C., Jouanno, J., Gaillard, F., Kolodziejczyk, N., Maes, C., Reul, N., et al. (2017). Importance of the Equatorial Undercurrent on the sea surface salinity in the eastern equatorial Atlantic in boreal spring. *Journal of Geophysical Research: Oceans*, 122, 521–538. https://doi. org/10.1002/2016JC012342

Dadou I., Garçon, V., Andersen, V. , FlierI, G. R., & Davis, C. S. (1996), Impact of the North Equatorial Current meandering on a pelagic ecosystem: A modeling approach, *Journal of Marine Research*, 54, 311-342

de Boyer Montégut, C., Madec, G., Fischer, A. S., Lazar, A., & Iudicone, D. (2004), Mixed layer depth over the global ocean: An examination of profile data and a profile-based climatology, J. *Geophys. Res*., 109, C12003, doi:10.1029/2004JC002378.

Delpech, A., Cravatte, S., Marin, F., Morel, Y. Gronchi, E., & Kestenare, E. (2020), Observed Tracer Fields Structuration by Middepth Zonal Jets in the Tropical Pacific. *J. Phys. Oceanogr*. 50, 281–304, doi:10.1175/JPO-D-19-0132.1.

Ducet N., Le Traon P.-Y., & Reverdun, G. (2000), Global high-resolution mapping of ocean circulation from TOPEX/Poseidon and ERS-1 and -2, *J. Geophys. Res*. 105 (C8), 19,477-19,498.

Emery, W. J. (2003), Water Types and Water Masses, Ocean Circulation, pp. 1556–1567, *Elsevier Sci., Amsterdam, Netherlands*

Emery, W.J., & Meincke, J. (1986), Global water masses: summary and review. Oceanol. Acta 9 (4). 344-383.

Ertel, H. (1942), On hydrodynamic eddy theorems. Physikalische Zeitschrift 43, 526–529.

Foltz, G. R., Brandt, P., Richter, I., Rodriguez-Fonseca, B., Hernandez, F., Dengler, M., et al. (2019), The Tropical Atlantic Observing System. *Front. Mar. Sci*. 6:206. doi: 10.3389/fmars.2019.00206

Foussard, A., Lapeyre G., & Plougonven R. (2019), Response of Surface Wind Divergence to Mesoscale SST Anomalies under Different Wind Conditions, *Journal of the Atmospheric Sciences*, *76*(7), 2065–2082, doi:10.1175/jas-d-18-0204.1.

Frenger, I., Gruber N. , Knutti R., & Münnich M. (2013), Imprint of Southern Ocean eddies on winds, clouds

and rainfall, *Nature Geoscience*, *6*(8), 608–612, doi:10.1038/ngeo1863.

Garraffo, Z. D., Johns, W. E., Chassignet, E. P., & Goni, G. J. (2003), North Brazil Current rings and transport of southern waters in a high resolution numerical simulation of the North Atlantic. In G. J. Goni & P. Malanotte Rizzoli (Eds.), Interhemispheric Water exchange in the Atlantic Ocean, *Elsevier Oceanographic Series* 68 (pp. 375–409). Amsterdam: Elsevier.

Gaube, P., Mcgillicuddy, D. J., Chelton, D. B., Behrenfeld M. J., &Strutton, P. G. (2014), Regional variations in the influence of mesoscale eddies on near-surface chlorophyll, *Journal of Geophysical Research: Oceans*, *119*(12), 8195–8220, doi:10.1002/2014jc010111.

Gentemann, C. L., Minnett, P. J., Le Borgne, P., & Merchant, C. J. (2008), Multi-satellite measurements of large diurnal warming events, *Geophys. Res. L ett.*, 35, L2260 2, doi:10.1029/2008GL035730.

Guemas, V., Salas-Mélia, D., Kageyama, M., Giordani, H., & Voldoire, A. (2011), Impact of the ocean mixed layer diurnal variations on the intraseasonal variability of Sea Surface Temperatures in the Atlantic Ocean. *J. Climate* 24 (12), 2889–2914, http://dx.doi.org/10.1175/2010JCLI3660.1

Gula, J., Molemaker M., & McWilliams, J. (2015), Topographic vorticity generation, submesoscale instability and vortex street formation in the Gulf Stream. *Geophys. Res. Lett*. 42, 4054–4062.

Gula, J., Molemaker, M., & McWilliams, J. (2016), Topographic generation of submesoscale centrifugal instability and energy dissipation. *Nat. Commun*. 7, 12811, doi:10.1038/ncomms12811.

Haynes, P., & McIntyre, M. (1987), On the evolution of vorticity and potential vorticity in the presence of diabatic heating and frictional or other forces. *J. Atmos. Sci.* 44 (5), 828–841.

Haynes, P., McIntyre, M. (1990), On the conservation and impermeability theorems for potential vorticity. *J. Atmos. Sci*. 47 (16), 2021–2031.

Herbette S., Morel Y. & Arhan M. (2004), Subduction of a Surface vortex under an outcropping front. *J. Phys. Ocean*. 34, pp. 1610-1627.

Herbette S., Morel Y. & Arhan M. (2003), Erosion of a surface vortex by a seamount. *J. Phys. Oceanogr.* 33, 1664– 1679

886 Holmes, R.M., & Thomas, L.N. (2016), Modulation of Tropical Instability Wave Intensity by Equatorial Kelvin
887 Waves. *J. Phys. Oceanogr*. 46, 2623–2643, doi:10.1175/JPO-D-16-0064.1.
888 Holmes, R. M., Thomas, L.N., Thompson, L., & Darr, D. (2014), Potential Vorticity Dynamics of Tropical
889 Instability Vortices. *J. Phys. Oceanogr.* 44, 995–1011, doi:10.1175/JPO-D-13-0157.1.
890 Hormann, V., & Brandt P. (2007), Atlantic equatorial undercurrent and associated cold tongue variability, *J.*
891 *Geophys. Res.*, 112, C06017, doi:10.1029/2006JC003931.
892 Hoskins, B.J., McIntyre, M. E., & Robertson, A.W. (1985), On the use and significance of isentropic
893 potential vorticity maps. *Q. J. R. Met. Soc*. 470, 877–946.
894 Itoh, S., & I. Yasuda (2010), Water Mass Structure of Warm and Cold Anticyclonic Eddies in the Western
895 Boundary Region of the Subarctic North Pacific, *Journal of Physical Oceanography*, *40*(12), 2624–
896 2642, doi:10.1175/2010jpo4475.1.
897 Ioannou A., Stegner A., Dumas F., & Le Vu B. (2020), Three-Dimensional Evolution of Mesoscale
898 Anticyclones in the Lee of Crete, *Frontiers in Marine Science*, 7, 1019, doi:10.3389/fmars.2020.609156
899 Kelly, B., Meyers S. & O'Brien J. (1995), On a generating mechanism for Yanai waves and the 25-day
900 oscillation, *J. Geophys. Res*., 100, 10,589 – 10,612.
901 Keppler, L., Cravatte S., Chaigneau A., Pegliasco C., Gourdeau L., & Singh A. (2018), Observed Characteristics
902 and Vertical Structure of Mesoscale Eddies in the Southwest Tropical Pacific, *Journal of Geophysical*
903 *Research: Oceans*, *123*(4), 2731–2756, doi:10.1002/2017jc013712.
904 Kirchner, K., Rhein M., Hüttl-Kabus S. & Böning C. W. (2009), On the spreading of South Atlantic Water
905 into the northern hemisphere. *J. Geophys. Res*., 114, C05019, doi:10.1029/ 2008JC005165
906 Kolodziejczyk, N., Bourlès B., Marin F., Grelet J. & Chuchla R. (2009), Seasonal variability of the Equatorial
907 Undercurrent at 10°W as inferred from recent in situ observations, *J. Geophys. Res*., 114, C06014,
908 doi:10.1029/2008JC004976.
909 Kurian, J., F. Colas, X. Capet, J. C. McWilliams, and D. B. Chelton (2011), Eddy properties in the California
910 Current System, J. Geophys. Res., 116, C08027, doi:10.1029/2010JC006895.

911 Laxenaire, R., Speich S., Blanke B., Chaigneau, A., Pegliasco C., & Stegner A. (2018), Anticyclonic Eddies
912 Connecting the Western Boundaries of Indian and Atlantic Oceans, *Journal of Geophysical Research:*
913 *Oceans*, *123*(11), 7651–7677, doi:10.1029/2018jc014270.
914 Laxenaire, R., Speich, S., & Stegner, A. (2020), Agulhas ring heat content and transport in the South Atlantic
915 estimated by combining satellite altimetry and Argo profiling floats data. *Journal of Geophysical*
916 *Research*: Oceans, 125, e2019JC015511. https:// doi.org/10.1029/2019JC015511
917 Le Traon P.-Y., Nadal, F., & Ducet, N. (1998), An Improved Mapping Method of Multisatellite Altimeter Data,
918 *J. Atmos. Oceanic Technol*. 15, 522-534
919 Liu, M. & Tanhua, T. (2019), Characteristics of Water Masses in the Atlantic Ocean based on GLODAPv2
920 data, *Ocean Sci. Discuss.*, https://doi.org/10.5194/os-2018-139, in review.
921 Locarnini, R. A., Mishonov, A. V., Baranova, O. K. et al. (2018), *World Ocean Atlas 2018, Volume 1:*
922 *Temperature.* A. *Mishonov Technical Ed*.; NOAA Atlas NESDIS 81, 52 pp.
923 Martínez-Marrero, A., Rodríguez-Santana A., Hernández-Guerra A., Fraile-Nuez, E., López-Laatzen, F., Vélez-
924 Belchí, P., & Parrilla, G. (2008), Distribution of water masses and diapycnal mixing in the Cape Verde
925 Frontal Zone, *Geophys. Res. Lett.*, 35, L07609, doi:10.1029/ 2008GL033229
926 McGillicuddy, D. J. (2016), Mechanisms of Physical-Biological-Biogeochemical Interaction at the Oceanic
927 Mesoscale, *Annual Review of Marine Science*, *8*(1), 125–159, doi:10.1146/annurev-marine-010814-
928 015606.
929 McWilliams, G. & Flierl, R. (1979), On the evolution of isolated, nonlinear vortices. *J. Phys. Oceanogr.*,
930 9, 1155–1182.
931 McWilliams, J. C. (1985), Submesoscale, coherent vortices in the ocean, *Rev. Geophys.*, 23(2), 165–
932 182, doi:10.1029/RG023i002p00165
933 Morel, Y. G., & McWilliams, J.C., (1997), Evolution of isolated interior vortices in the ocean, *J. Phys.*
934 *Oceanogr*. 27, 727–748.
935 Morel, Y., Gula J., & Ponte A. (2019), Potential vorticity diagnostics based on balances between volume integral

and boundary conditions, *Ocean Modelling*, *138*, 23–35, doi:10.1016/j.ocemod.2019.04.004.

Morel, Y., & McWilliams J. (2001), Effects of isopycnal and diapycnal mixing on the stability of oceanic currents. *J. Phys. Oceanogr.*, 31, 2280–2296.

Morel, Y., Darr D., & Tailandier, C., (2006), Possible sources driving the potential vorticity structure and long-wave instability of coastal upwelling and downwelling currents. *J. Phys. Ocean*. 36, 875–896.

Morel, Y., & Thomas, L. (2009), Ekman drift and vortical structures. *Ocean Model.* 27, 185–197

Morvan, M., L'Hégaret, P., Carton, X., Gula, J., Vic, C., de Marez, C., et al. (2019). The life cycle of submesoscale eddies generated by topographic interactions. Ocean Science, 15(6), 1531–1543. https://doi.org/10.5194/os-15-1531-2019

Muller, P. (2006), The Equations of Oceanic Motions; *Cambridge University Press: Cambridge, UK*.

Onken, R., & Klein, B. (1991), A model of baroclinic instability and waves between ventilated gyre and the shadow zone of the North Atlantic Ocean, *J. Phys. Oceanogr.*, 21, 53 – 67.

Pegliasco, C., Chaigneau, A., & Morrow, R. (2015), Main eddy vertical structures observed in the four major Eastern boundary upwelling systems: *J. Geophys. Res. Oceans*, 120, 6008- 6033.

Penney, J., Morel, Y., Haynes, P., Auclair, F., & Nguyen, C. (2020), Diapycnal mixing of passive tracers by Kelvin–Helmholtz instabilities. *Journal of Fluid Mechanics*, 900, A26. doi:10.1017/jfm.2020.483

Pérez-Rodriguez, P., Pelegri, J. L., & Marrero-Diaz, A. (2001), Dynamical characteristics of the Cape Verde frontal zone, *Sci. Mar.*, 65, 241–250.

Pujol, M.-I., Faugère, Y., Taburet, G., Dupuy, S., Pelloquin, C., Ablain, M., & Picot, N. (2016). DUACS DT2014: The new multi-mission altimeter data set reprocessed over 20 years. Ocean Science, 12(5), 1067–1090. https://doi.org/10.5194/os-12-1067-2016

Pullen, J., Doyle, J. D., May, P., Chavanne, C., Flament, P., & Arnone, R. A. (2008), Monsoon surges trigger oceanic eddy formation and propagation in the lee of the Philippine Islands. *Geophys. Res. Lett.* 35:L07604. doi: 10.1029/2007GL033109

Renault, L., Marchesiello, P., Masson, S., & McWilliams, J. C. (2019), Remarkable control of western boundary currents by Eddy Killing, a mechanical air-sea coupling process. *Geophysical Research Letters*, 46.

https://doi.org/10.1029/2018GL081211

Rugg, A., Foltz, G.R., & Perez, R.C. (2016), Role of mixed layer dynamics in tropical North Atlantic interannual sea surface temperature variability. *J. Clim*. 29 (22), 8083–8101.

Saenko, O. A., Yang, D., & Gregory, J. M. (2018), Impact of mesoscale eddy transfer on heat uptake in an eddy parameterizing ocean model. *Journal of Climate*, 31(20), 8589–8606. https://doi.org/10.1175/jcli-d-18-0186.1

Schuckmann, K. V., Brandt, P., & Eden, C. (2008), Generation of tropical instability waves in the Atlantic Ocean, *Journal of Geophysical Research*, *113*(C8), doi:10.1029/2007jc004712.

Schütte, F., Brandt, P., & Karstensen, J. (2016), Occurrence and characteristics of mesoscale eddies in the tropical northeastern Atlantic Ocean, *Ocean Science*, *12*(3), 663–685, doi:10.5194/os-12-663-2016.

Seo, H., Miller, A., & Norris, J. (2016), Eddy-wind interaction in the California current system: Dynamics and impacts, *J. Phys. Oceanogr*., 46, 439–459, doi:10.1175/JPO-D-15-0086.1.

Snowden, D., & Molinari, R. (2003), Subtropical cells in the Atlantic Ocean: An observational summary, in Interhemispheric Water Exchange in the Atlantic Ocean, edited by G. Goni and P. Malanotte-Rizzoli, *Elsevier Oceanogr. Ser*., 68, 287 – 312.

Sprintall, J., & Tomczak, M. (1993), On the formation of central water in the southern hemisphere. *Deep-Sea Research* 40, 827—848.

Stramma, L., & Schott, F. (1999), The mean flow field of the tropical Atlantic Ocean, *Deep Sea Res.* II, 46, 279 – 303.

Stramma, L., Juttl S., & Schafstall, J. (2005a), Water masses and currents in the upper tropical northeast Atlantic off northwest Africa, *J. Geophys. Res.*, 110, C12006, doi:10.1029/2005JC002939.

Stramma, L., M. Rhein, Brandt, P., Dengler, M., Böning, C. & Walter, M. (2005b), Upper ocean circulation in the western tropical Atlantic in boreal fall 2000, Deep Sea Res., I, (52), 221 – 240.

Sun, B., Liu, C. & Wang, F. (2019), Global meridional eddy heat transport inferred from Argo and altimetry observations. *Sci Rep* **9,** 1345. https://doi.org/10.1038/s41598-018-38069-2

Sun, W., Dong, C., Tan, W., Liu, Y., He, Y., & Wang, J. (2018), Vertical structure anomalies of oceanic eddies and eddy-induced transports in the South China Sea. *Remote Sens.* 10, 795. https://doi.org/10.3390/rs10050795

Sutyrin G. G. & Flierl, G. R. (1994), Intense vortex motion on the beta-plane: development of the beta-gyres, J. *Atmos. Sci.* 51, 773–790

Sutyrin G.G. & Morel, Y.G. (1997), Intense vortex motion in a stratified fluid on the beta-plane: an analytical theory and its validation, *J. Fluid Mech*. 336, 203–220.

Sverdrup, H.U., Johnson, M.W., & Fleming, R.H. (1942), The Oceans. Their Physics, Chemistry, and General Biology. *Prentice-Hall, Englewood Cliffs, NJ*, 1087 pp.

Thomas, L.N. (2005), Destruction of Potential Vorticity by Winds. *J. Phys. Oceanogr.*, 35, 2457–2466, doi:10.1175/JPO2830.1.

Thomas, M. D., & Zhai, X. (2013), Eddy-induced variability of the meridional overturning circulation in a model of the North Atlantic, *Geophys. Res. Lett.*, 40, 2742–2747, doi:10.1002/grl.50532

Tiedemann, M., Fock, H. O., Döring, J., Badji, L. B. & Möllmann, C. (2018), Water masses and oceanic eddy regulation of larval fish assemblages along the Cape Verde frontal zone. *J. Mar. Syst*., 183, 42–55.

Tomczak, M., & Godfrey, J.S. (1994), Regional Oceanography: An Introduction. *Elsevier, Oxford,* 422 pp.

Tsuchiya, M., Talley, L. D., & McCartney, M. S. (1992), An eastern Atlantic section from Iceland southward across the equator, *Deep Sea Res.*, 39, 1885 – 1917

Urbano, D. F., De Almeida, R. A. F., & Nobre, P. (2008), Equatorial Undercurrent and North Equatorial Countercurrent at 38°W: A new perspective from direct velocity data. *J. Geophys. Res.*, 113, C04041, doi:10.1029/2007JC004215

Vandermeirsch, F., Morel, Y., & Sutyrin, G. (2001), The net advective effect of a vertically sheared current on a

coherent vortex. *J. Phys. Oceanogr.*, 31, 2210–2225.

Villas Bôas, A. B., Sato, O. T., Chaigneau, A. & Castelão, G. P. (2015), The signature of mesoscale eddies on the air sea turbulent heat fluxes in the South Atlantic Ocean, *Geophysical Research Letters*, *42*(6), 1856–1862, doi:10.1002/2015gl063105.

Wang, C. (2005), Subthermocline tropical cells and equatorial subsurface countercurrents. *Deep Sea Res. Part Oceanogr. Res. Pap*. 52, 123–135, doi:10.1016/j.dsr.2004.08.009.

Weisberg R. H., & Weingartner, T. J. (1988), Instability waves in the equatorial Atlantic Ocean, *Journal of Physical Oceanography*, 18, pp. 1641-1657

Wenegrat, J. O., & McPhaden, M. J. (2015), Dynamics of the surface layer diurnal cycle in the equatorial Atlantic Ocean (0, 23 W). *Journal of Geophysical Research: Oceans*, 120, 563–581. https://doi.org/10.1002/2014JC010504

Wilson, W., Johns, E., & Molinari, R. (1994), Upper layer circulation in the western tropical North Atlantic Ocean during August 1989, *J. Geophys. Res.*, 99, 22,513 – 22,523.

Xu, A., Yu, F. & Nan, F. (2019), Study of subsurface eddy properties in northwestern Pacific Ocean based on an eddy- resolving OGCM. *Ocean Dynamics* **69,** 463–474. https://doi.org/10.1007/s10236-019- 01255-5

Zenk, W., B. Klein, & Schröder, M. (1991), Cape Verde Frontal Zone, *Deep Sea Res., 38, suppl*. 1, S505-S530

Zweng, M. M., Reagan, J. R., Seidov, D. et al. (2018), World Ocean Atlas 2018, Volume 2: Salinity. *A. Mishonov Technical Ed.; NOAA Atlas NESDIS* 82, 50 pp.

Figures

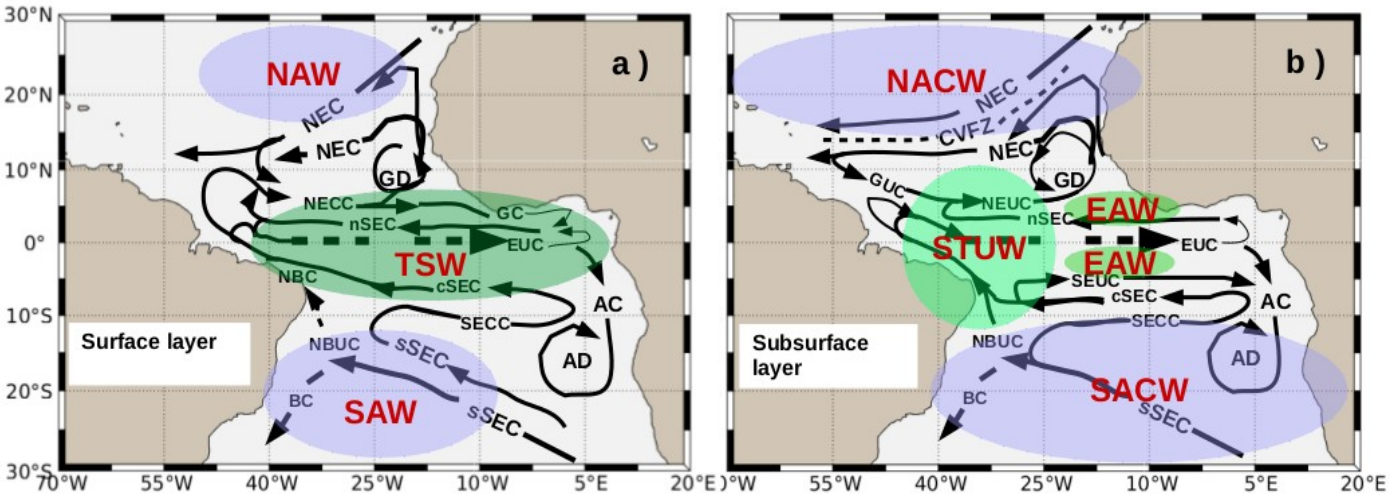

Figure 1. Schematic view of a) surface and b) subsurface circulation in the TAO (adapted from Stramma and Schott, 1999). Main currents are: Brazil Current (BC), North Brazil Current (NBC), North Brazil Undercurrent (NBUC), North Equatorial Current (NEC), North Equatorial Countercurrent (NECC), northern, central and southern branches of South Equatorial Current (nSEC, cSEC, sSEC), Guinea Current (GC), Angola Current (AC), Angola Dome (AD), Guinea Dome (GD), South Equatorial Countercurrent (SECC), Equatorial Undercurrent (EUC), North Equatorial Undercurrent (NEUC), South Equatorial Undercurrent (SEUC), Guiana Undercurrent (GUC). Tropical surface water-masses and central water-masses are also indicated: Tropical Surface water (TSW), Northern, southern and eastern tropical Atlantic water (NAW, SAW, EAW), Subtropical Underwater (STUW), North and South Atlantic Central Water (NACW, SACW).

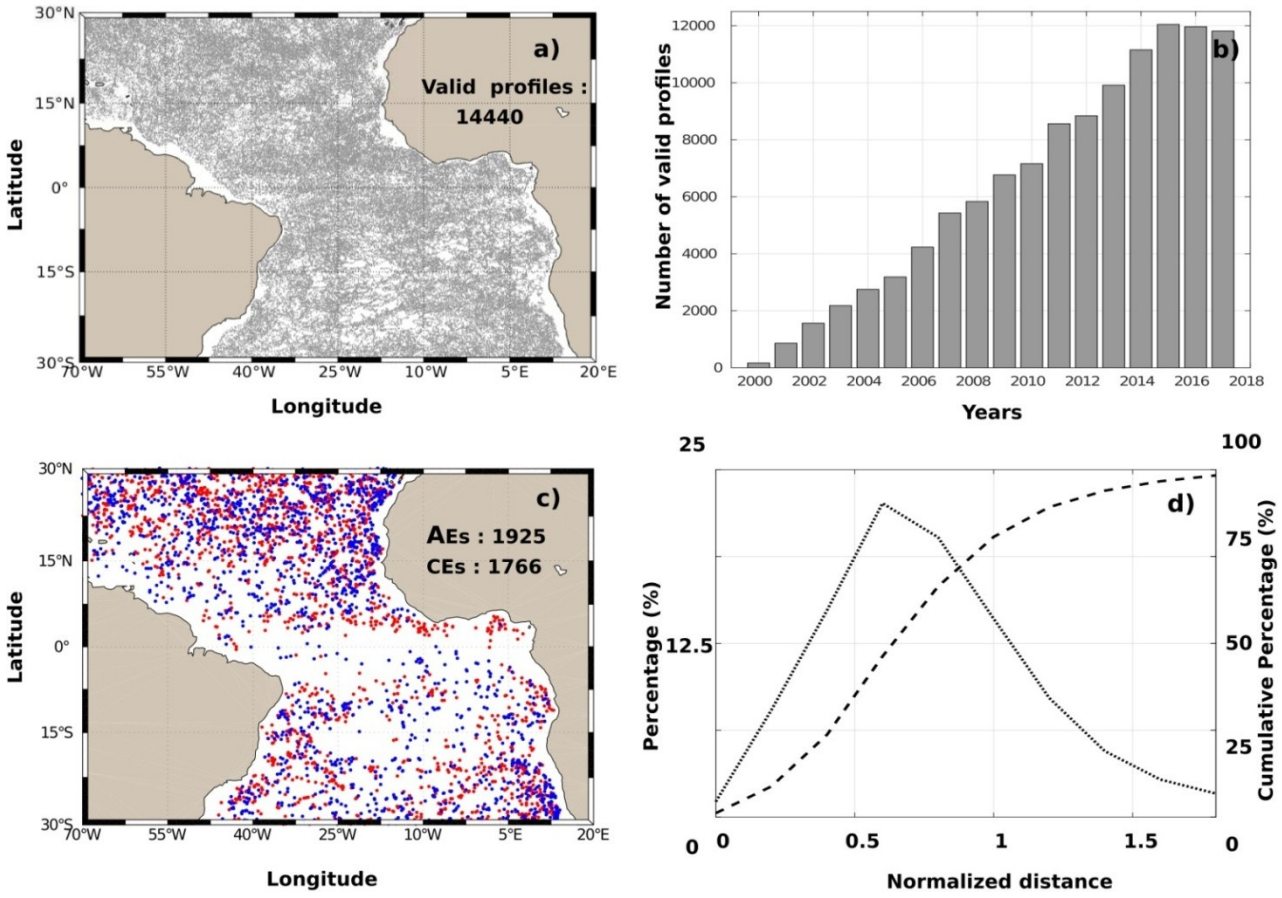

Figure 2. Spatio-temporal distribution of Argo floats in the TAO: a) Spatial and b) temporal distribution of valid Argo profiles, c) spatial distribution of Argo profiles that surfaced within anticyclonic eddies (AEs, red dots) and cyclonic eddies (CEs, blue dots), d) Histogram (dotted line, left axis) and cumulative distribution (dashed line, right axis) of the normalized radial distance of Argo floats to eddy centers. Normalized distances were obtained dividing the distance (in km) by the equivalent eddy radius.

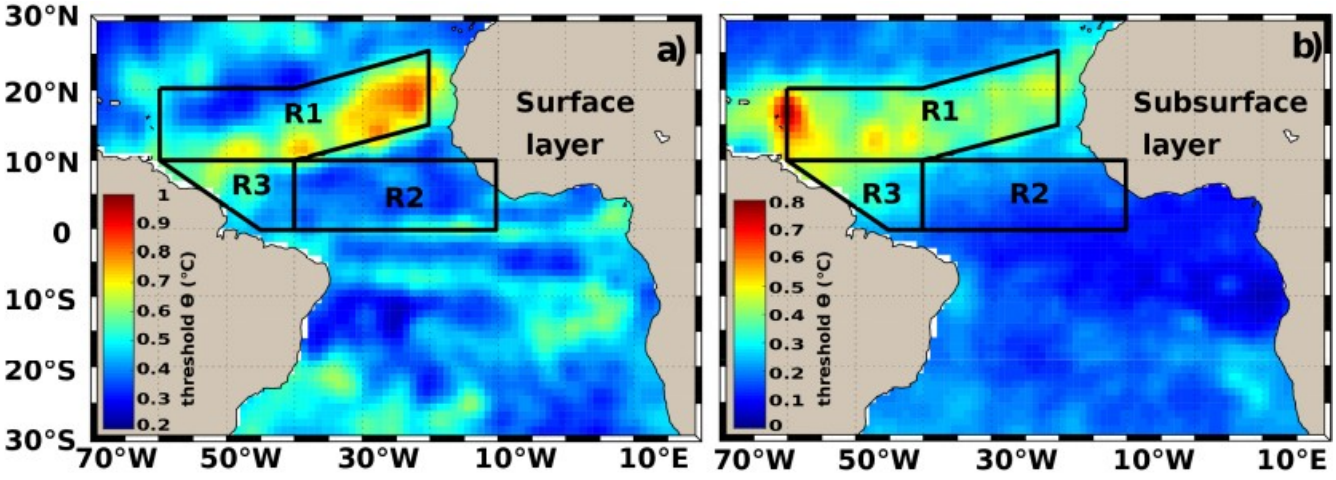

1054 Figure 3. Annual mean of the isopycnal temperature anomaly threshold within the a) surface and b) subsurface
1055 layers. Three dynamically different subregions (R1, R2, R3) used in this study are delimited in black (see in-text
1056 description of these regions). Surface layer extends from the mixed layer depth to the base of the pycnocline,
1057 whereas subsurface layer extends below the pycnocline to 1000 m depth.
1058
1059
1060

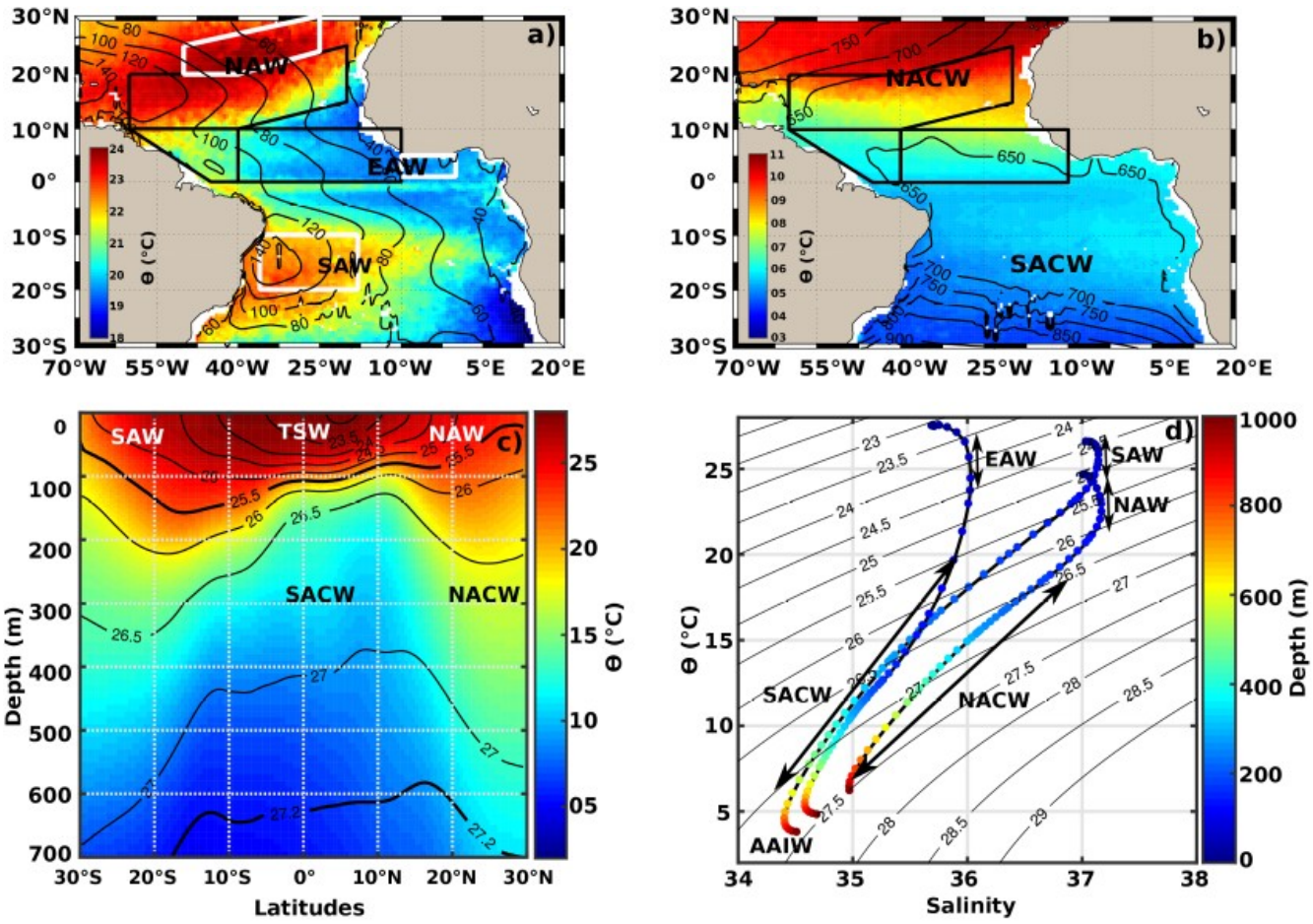

1062 Figure 4. Large-scale temperature distribution (in °C) on a) σ_θ= 25.5 kg m^{-3} and b) σ_θ= 27.2 kg m^{-3}. Black
1063 contours correspond to the depth (in m) of the corresponding σ_θ layer, whereas black boxes delimit the R1-R3
1064 subregions. c) Mean meridional temperature section along 35°W; black contours depict σ_θ levels. d) Mean *θ/S*
1065 diagram and main water-masses observed within the 3 white boxes delimited in a). Water-masses: NAW: North
1066 Atlantic Water; SAW: South Atlantic Water; TSW: Tropical Surface Water; EAW: Eastern Atlantic Water;
1067 NACW: North Atlantic Central Water; SACW: South Atlantic Central Water; AAIW: Antarctic Intermediate
1068 Water.
1069
1070
1071

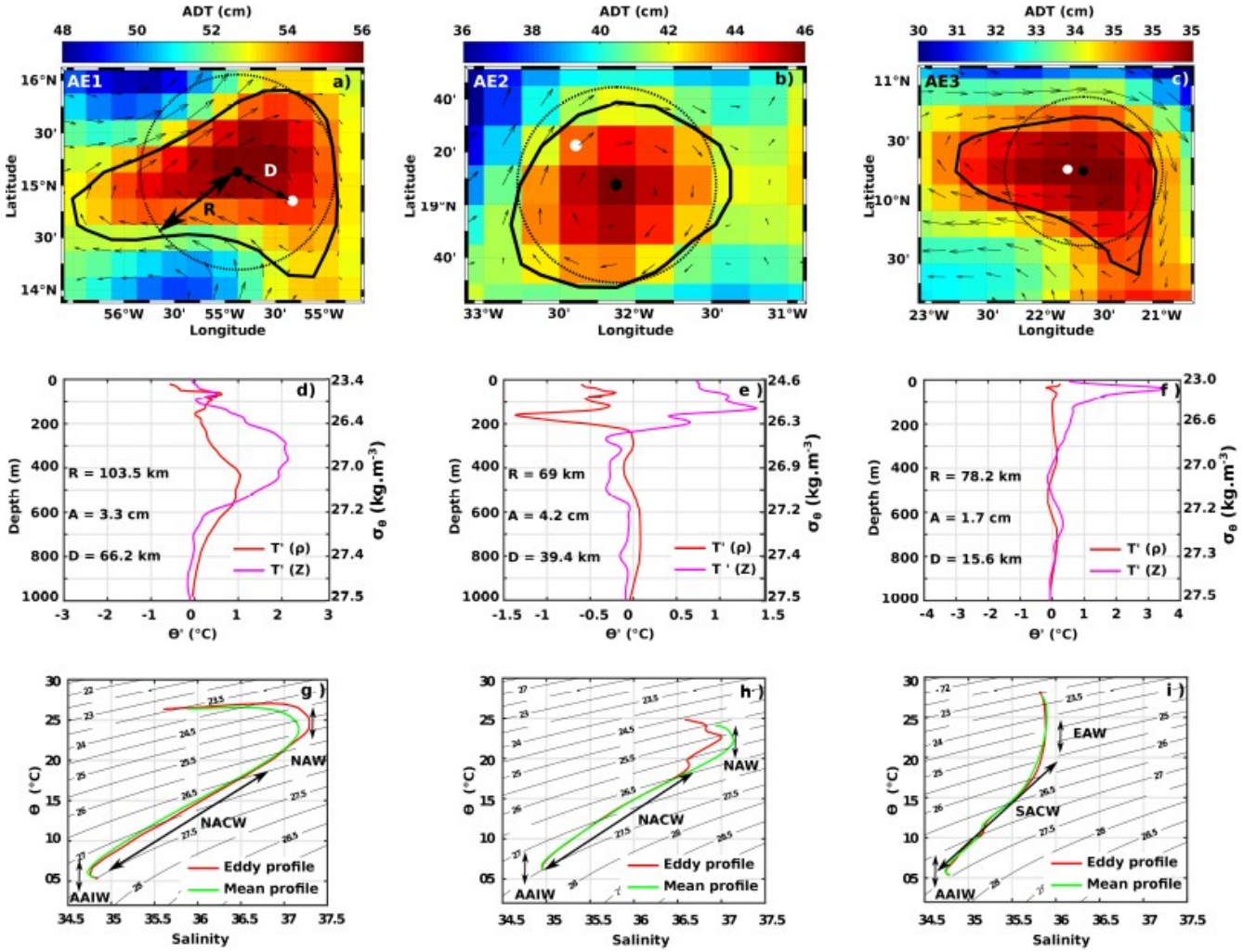

Figure 5. Density-coordinate anomalies compared to depth-coordinate anomalies for three case-study anticyclonic eddies. a-c) Eddy characteristics in AVISO maps. Black and white dots correspond to the eddy centers and the location of surfaced Argo floats, respectively, black contours delimit eddy edges whereas dotted circles represent the contours of the disc corresponding to eddy areas. d-f) Temperature anomalies observed within eddies in depth-coordinates (magenta lines) and in density-coordinates (red lines). R, A and D indicate the eddy radius, amplitude and the distance of the surfaced Argo float to the eddy center. g-i) θ-S diagram obtained within eddies (red lines) and for the mean climatology at the same location (green curves). Water-masses: NAW: North Atlantic Water; EAW: Eastern Atlantic Water; NACW: North Atlantic Central Water; SACW: South Atlantic Central Water; AAIW: Antarctic Intermediate Water.

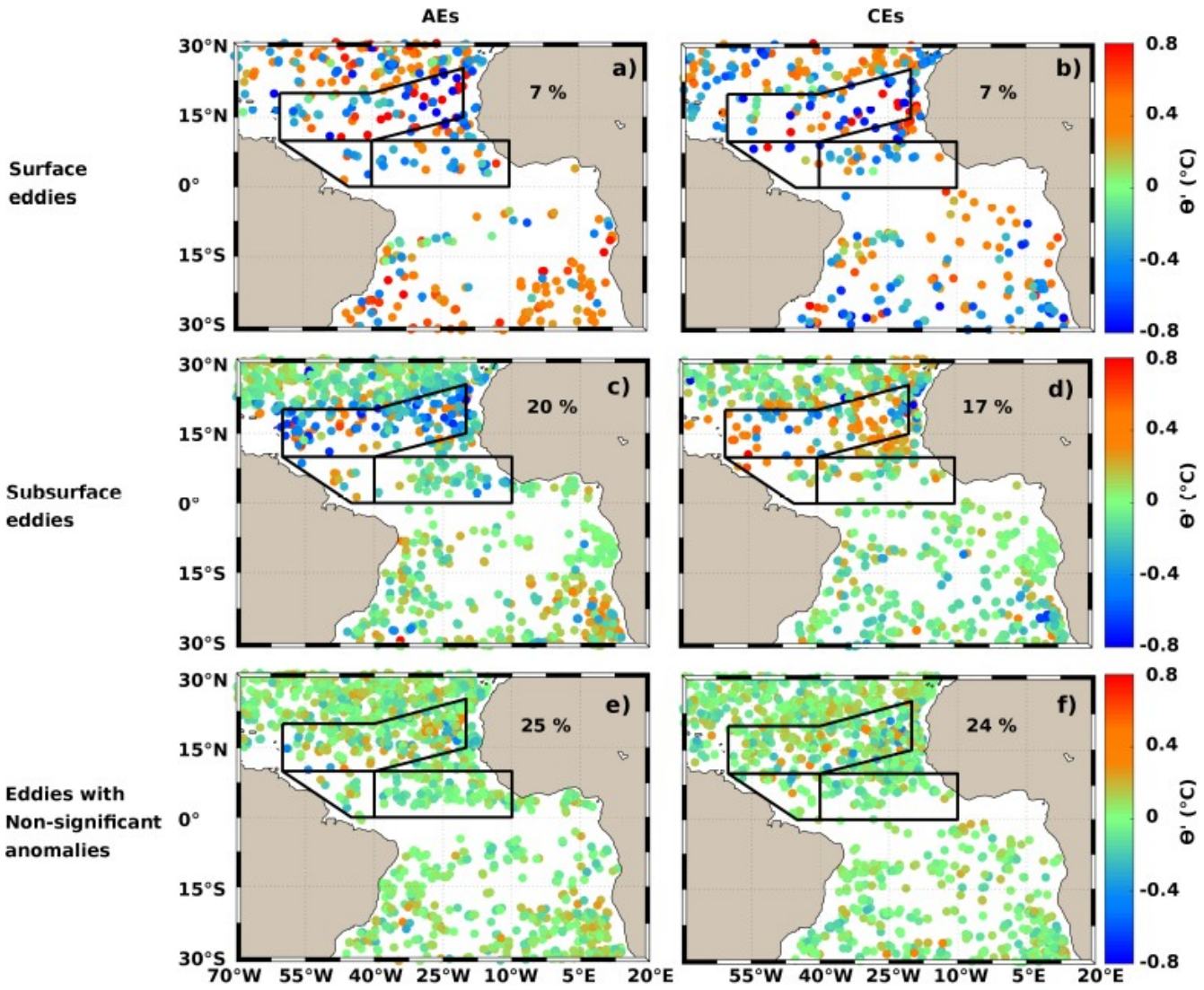

Figure 6. Spatial distribution of isopycnal temperature anomalies within new-born eddies. a-b) Significant surface θ' within AEs and CEs. c-d) Significant subsurface θ' within AEs and CEs. e-f) non-significant θ' within AEs and CEs. Black boxes delimit the R1-R3 subregions. Numbers indicate the percentage of sampled eddies for each category.

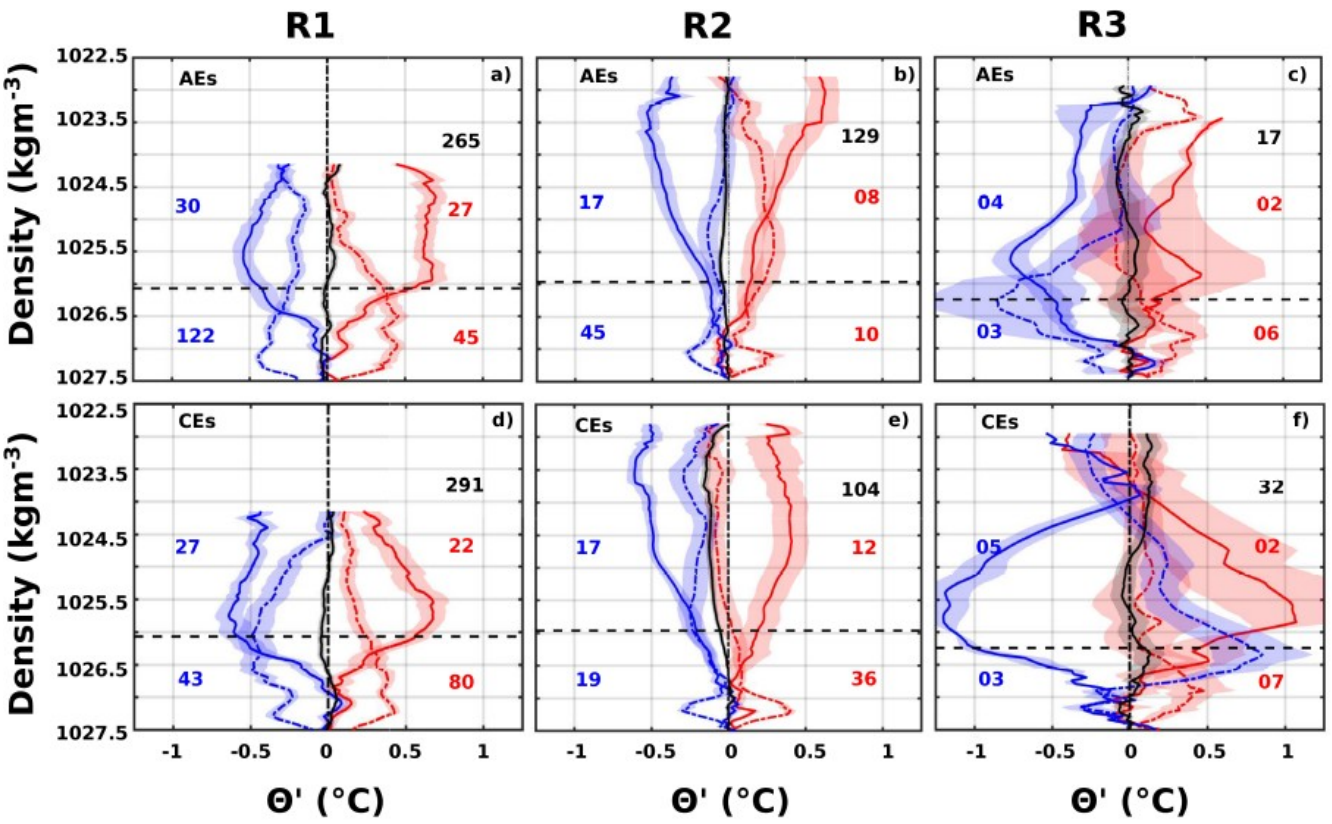

Figure 7. Mean isopycnal temperature structures of newborn a-c) anticyclonic (AEs) and d-f) cyclonic (CEs) eddies within 3 sub-regions (R1-R3.) Significant surface and subsurface anomalies are represented in solid and dashed lines, respectively, whereas positive anomalies are in red and negative anomalies in blue. Non-significant anomalies are represented in black. For each subplot, black numbers indicate the number of sampled eddies having non-significant θ', the right red top (bottom, respectively) numbers indicate the number of surface (subsurface) eddies with positive anomalies and the left blue top (bottom, respectively) numbers indicate the number of surface (subsurface) eddies with negative anomalies. Shading areas correspond to standard errors of the means, evaluated using Student's t test with a significance level of 95%. For each subregion, the horizontal dashed line corresponds to the base of the pycnocline that delimits the surface and subsurface layers.

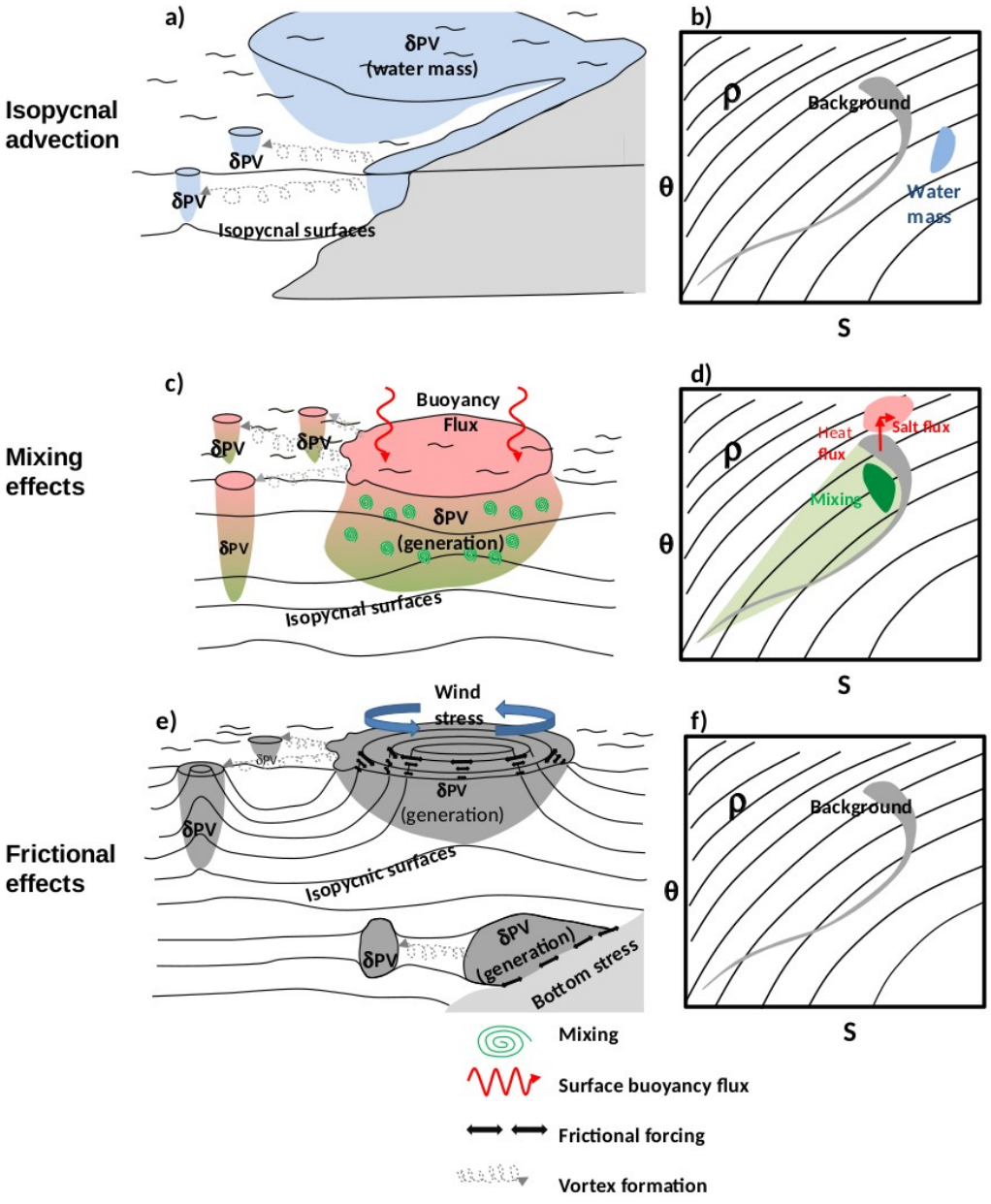

Figure 8. Qualitative analysis of the combined effects of specific mechanisms on the creation of PV (left column) and corresponding *θ/S* diagrams (right column). a-b) Advection of specific water-mass (in blue) in a region with different PV and *θ/S* characteristics (in white/black). c-d) Creation of PV anomalies by diapycnal mixing (green) and atmospheric buoyancy fluxes (red); These mechanisms also create *θ/S* anomalies. e-f) Frictional effects associated with surface wind or bottom stress; This mechanism is the only one that does not create *θ/S* anomalies. *θ/S* diagrams representative of the background are in black.

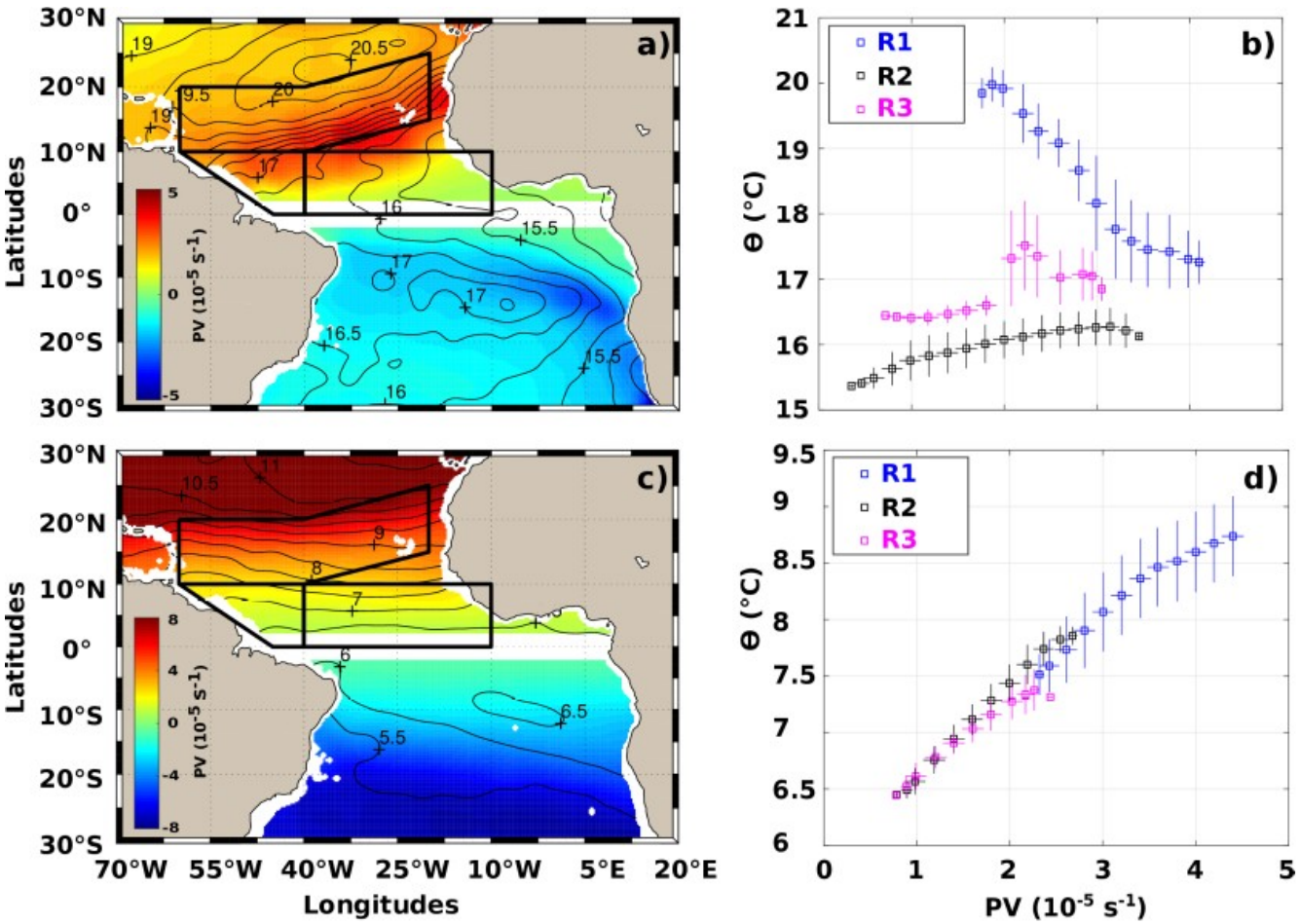

1128 Figure 9. Large-scale rescaled potential vorticity (PV, color shading) and θ (in °C, black contours), averaged
1129 between a) σ_θ = 25.75 - 26.5 kg m^{-3} and c) σ_θ = 26.9 - 27.4 kg m^{-3}. Black boxes delimit the R1-R3 subregions. b
1130 & d) PV/θ relationships in R1-R3 subregions. PV (and corresponding θ) were averaged in intervals of 0.2x10^{-5}s^{-1}
1131 (dots) and the corresponding standard deviations are indicated by solid lines.
1132
1133

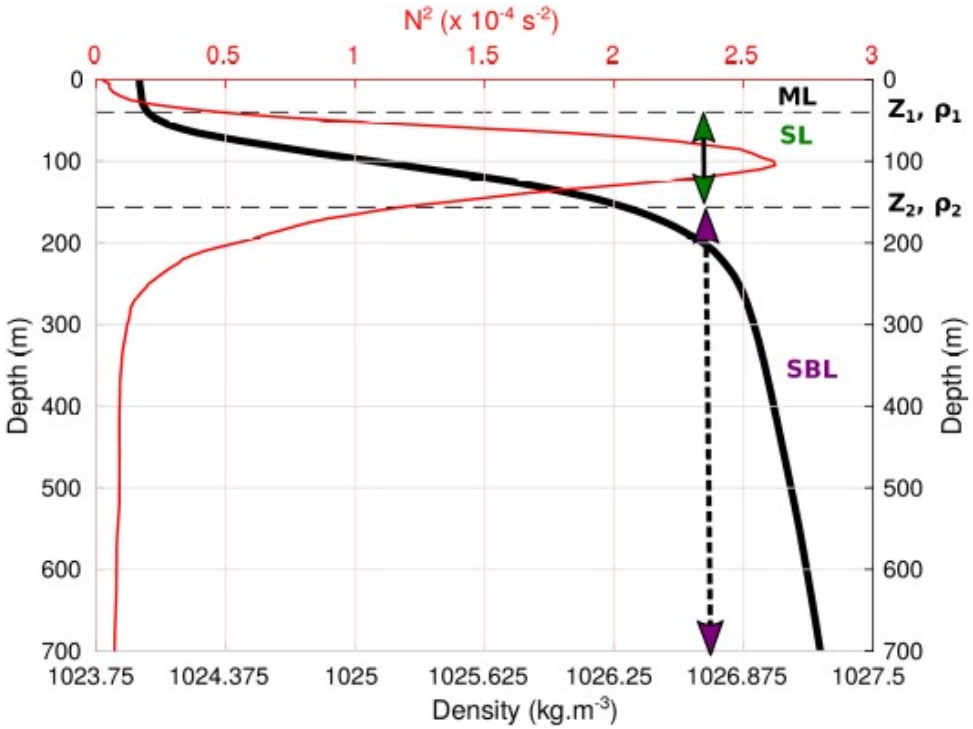

Figure A1. Mean density (black curve) and square buoyancy frequency (N^2, red curve) profiles at a given grid location showing the mixed (ML), surface (SL) and subsurface (SBL) layers. (Z_1, ρ_1) and (Z_2, ρ_2) are the mixed layer and the base of the pycnocline depths and densities.

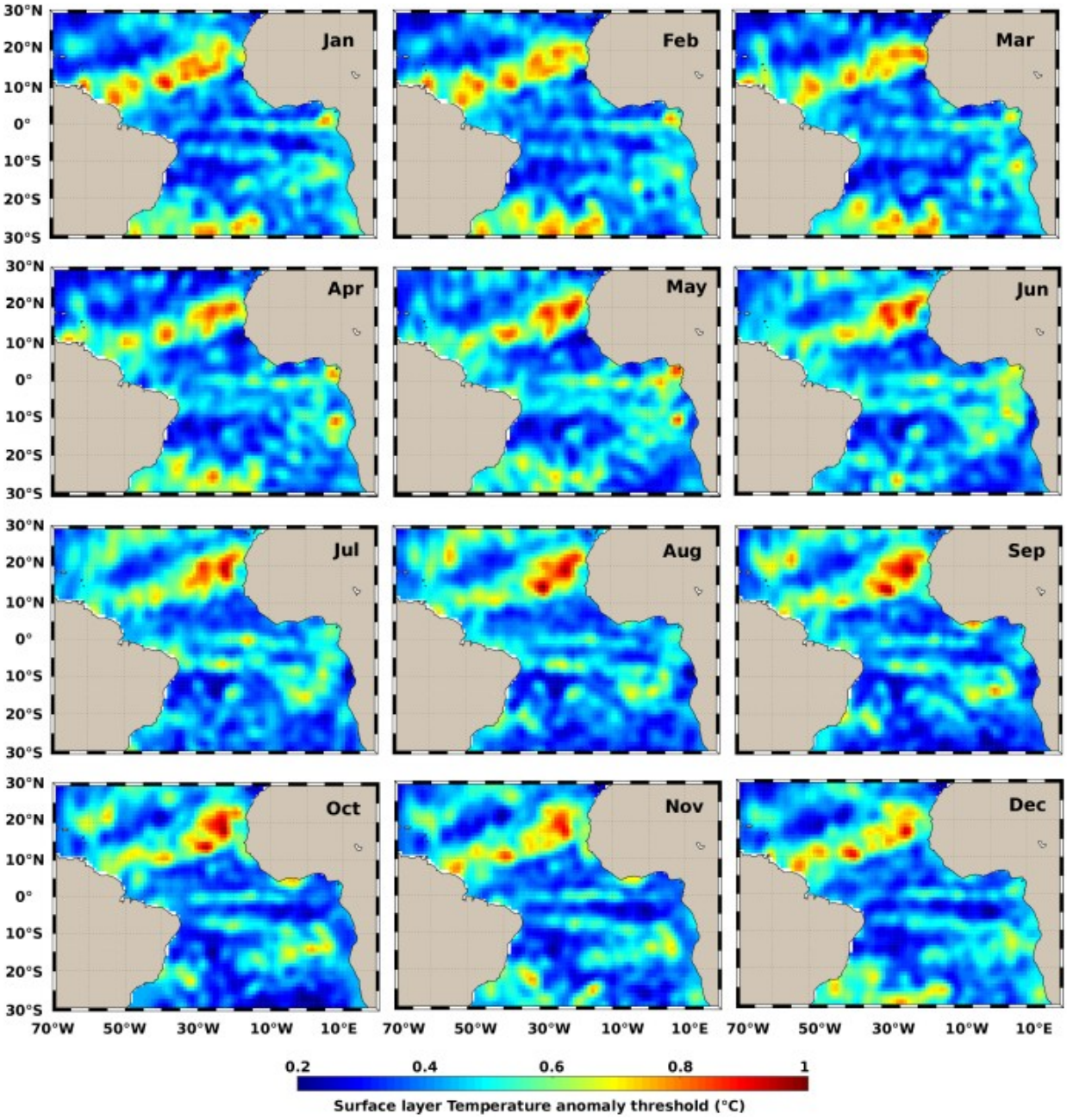

Figure A2. Monthly mean of the temperature anomaly threshold within the surface layer.

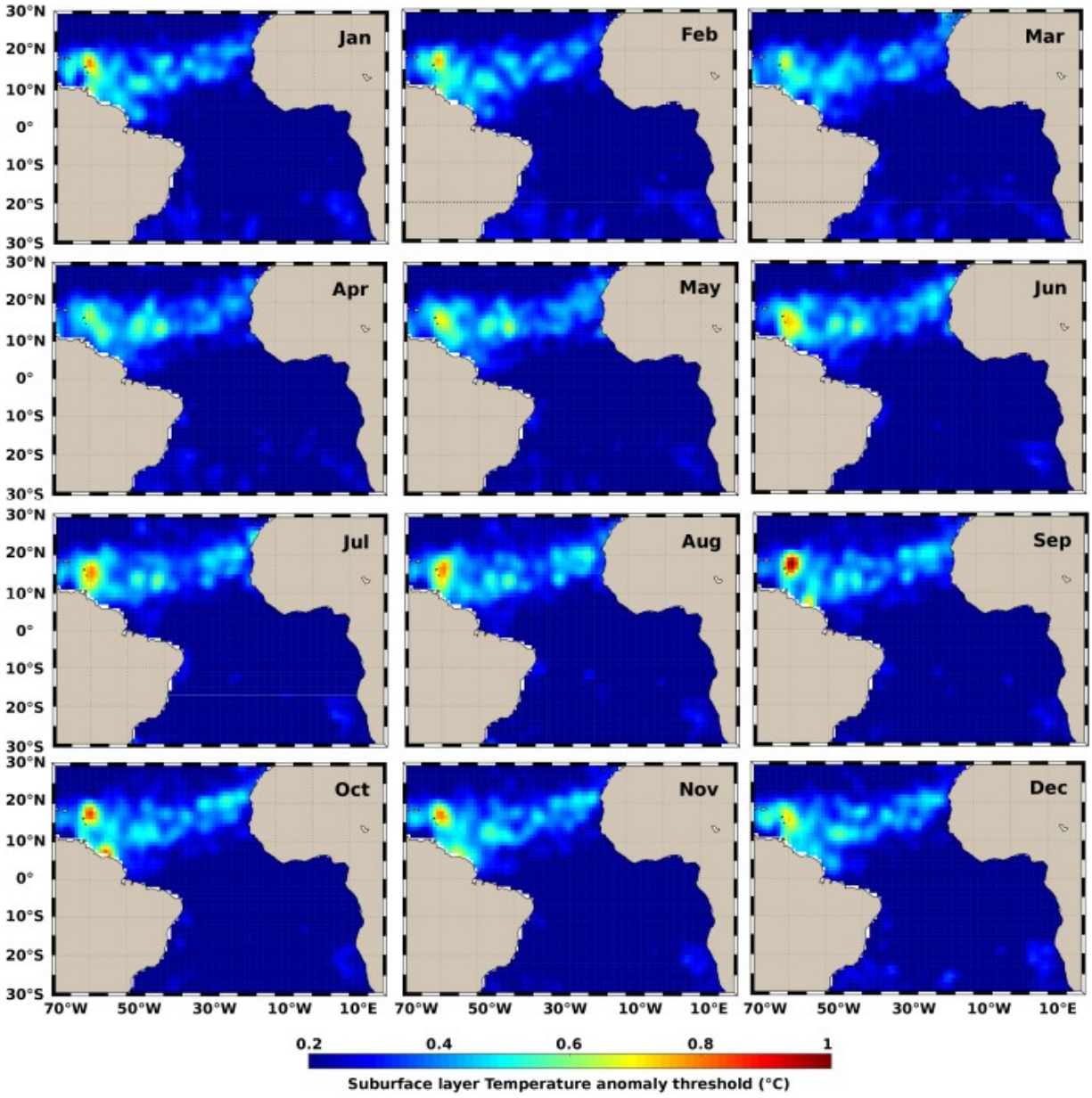

Figure A3. Monthly mean of the temperature anomaly threshold within the subsurface layer.

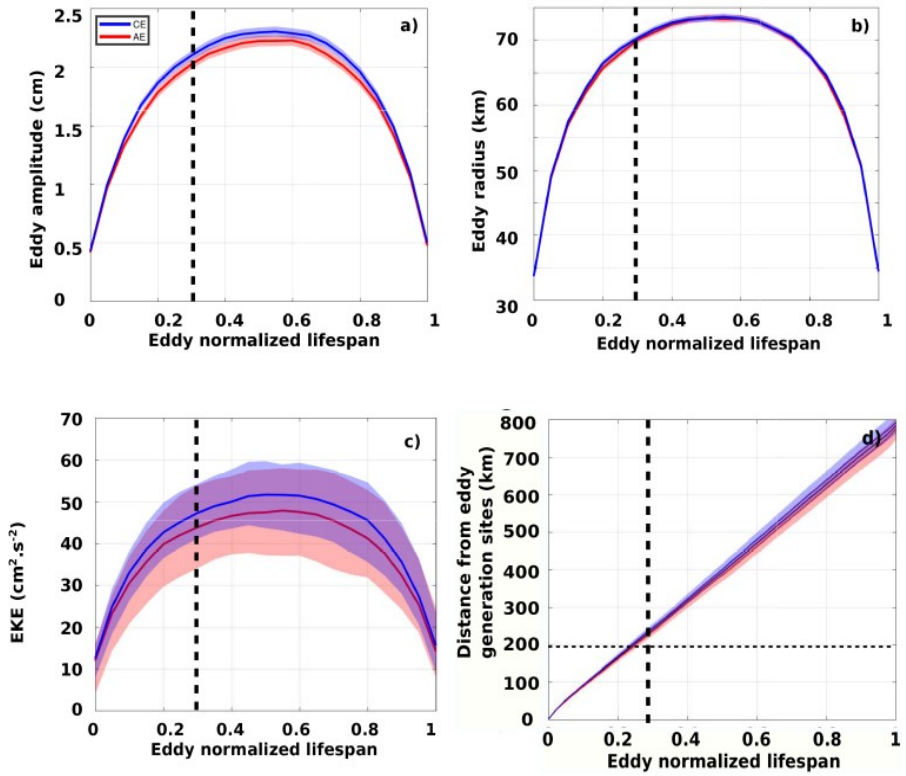

Figure A4. Mean eddy a) amplitude, b) radius, c) kinetic energy (EKE) and d) propagation distance as a function of normalized lifespan. Vertical dashed lines delimit the eddy growth phase from the mature phase, and correspond to 30% of eddy lifespan and the horizontal dashed line indicates the 200 km distance. Shading areas correspond to standard errors around the mean.

Figure1.

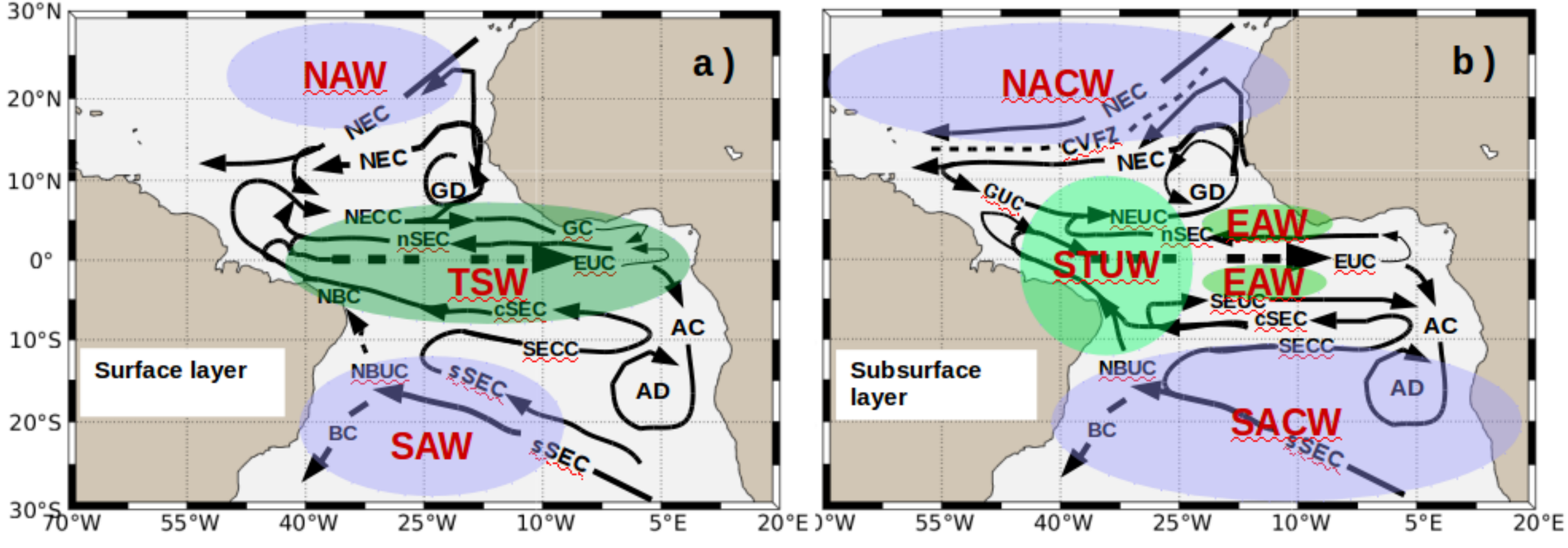
a)
NAW
NEC
NEC
GD
NECC
GC
nSEC
EUC
TSW
NBC
cSEC
AC
SECC
AD
NBUC
sSEC
BC
SAW
sSEC
Surface layer
b)
NACW
NEC
CVFZ
NEC
GUC
GD
NEUC
EAW
nSEC
STUW
EUC
EAW
SEUC
cSEC
AC
SECC
NBUC
AD
BC
SACW
sSEC
Subsurface layer
30°N
20°N
10°N
0°
10°S
20°S
30°S
70°W
55°W
40°W
25°W
10°W
5°E
20°E

Figure2.

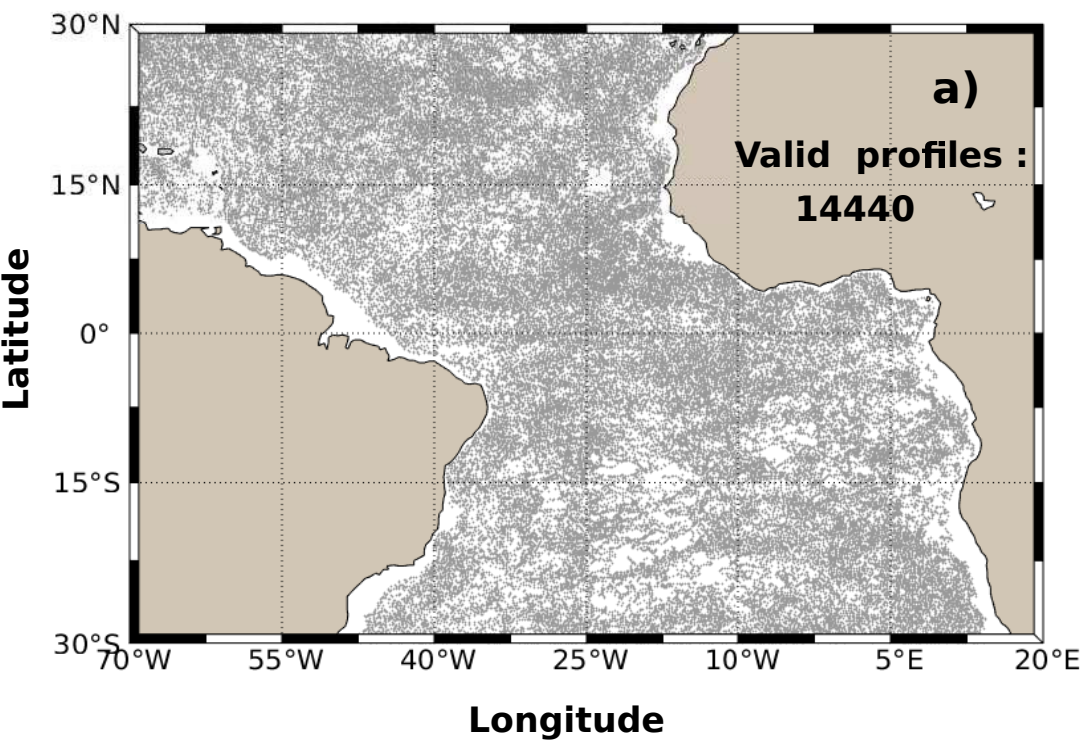
a)
Valid profiles :
14440
30°N
15°N
0°
15°S
30°S
70°W
55°W
40°W
25°W
10°W
5°E
20°E
Latitude
Longitude

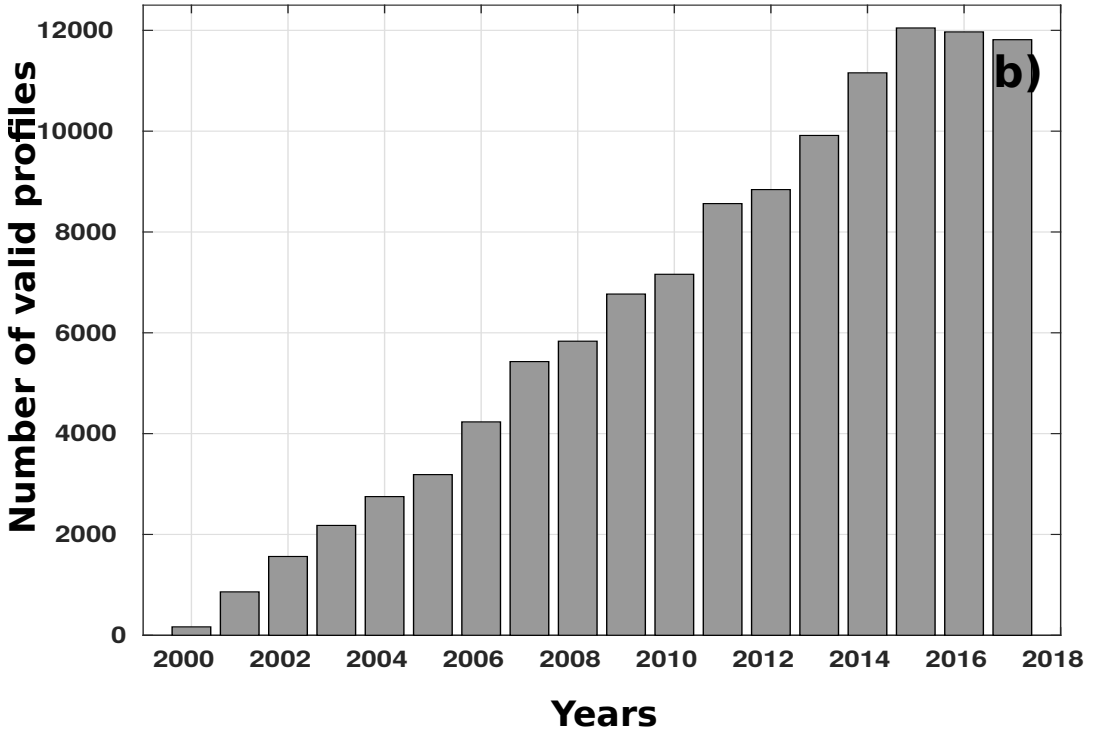
b)
Number of valid profiles
12000
10000
8000
6000
4000
2000
0
2000
2002
2004
2006
2008
2010
2012
2014
2016
2018
Years

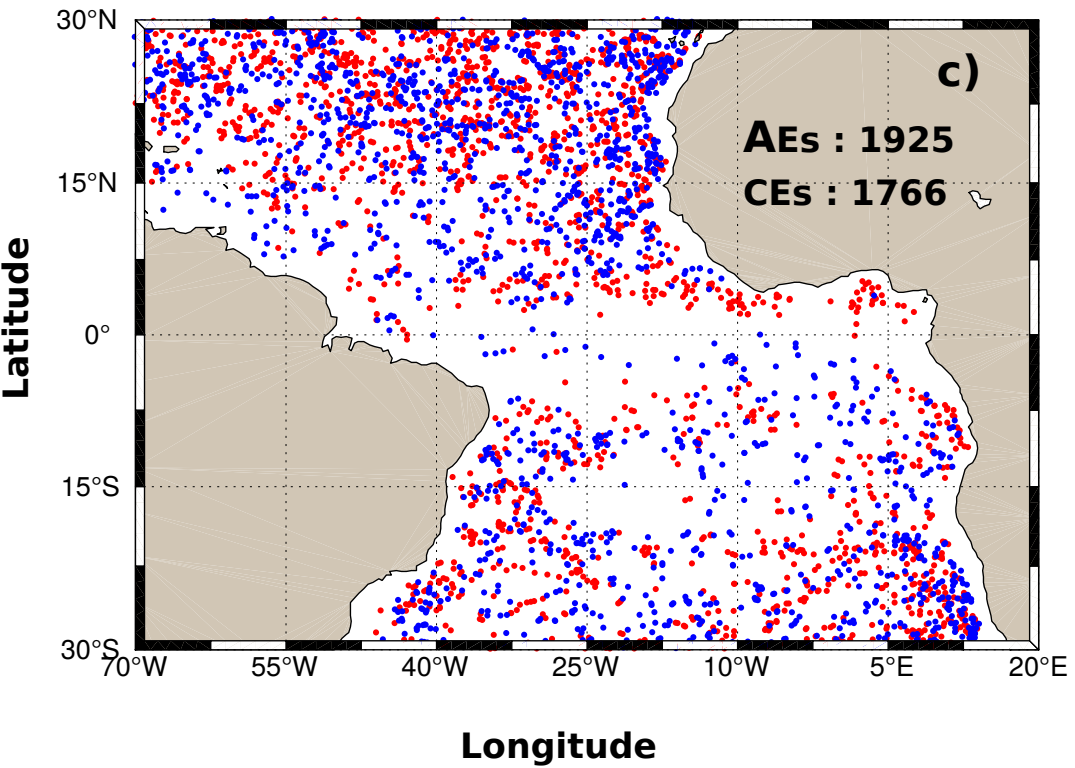
c)
AEs : 1925
CEs : 1766
30°N
15°N
0°
15°S
30°S
70°W
55°W
40°W
25°W
10°W
5°E
20°E
Latitude
Longitude

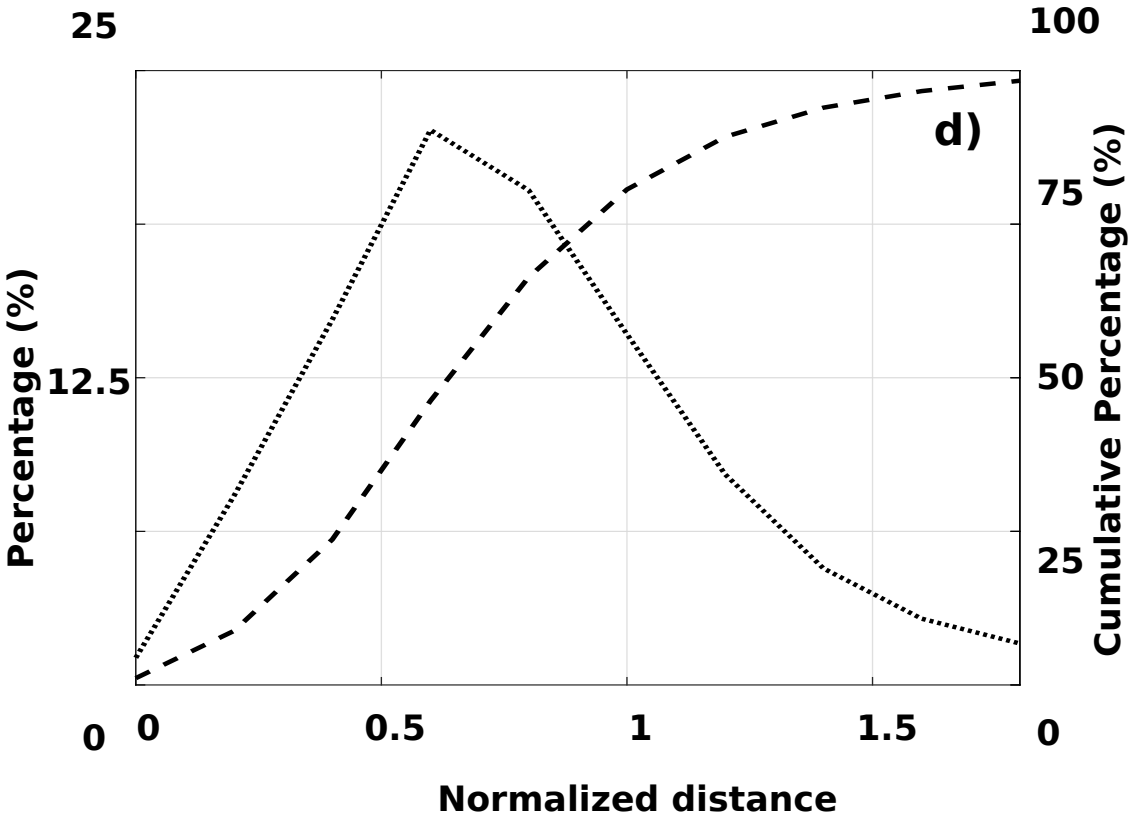
d)
25
12.5
0
Percentage (%)
100
75
50
25
0
Cumulative Percentage (%)
0
0.5
1
1.5
Normalized distance

Figure3.

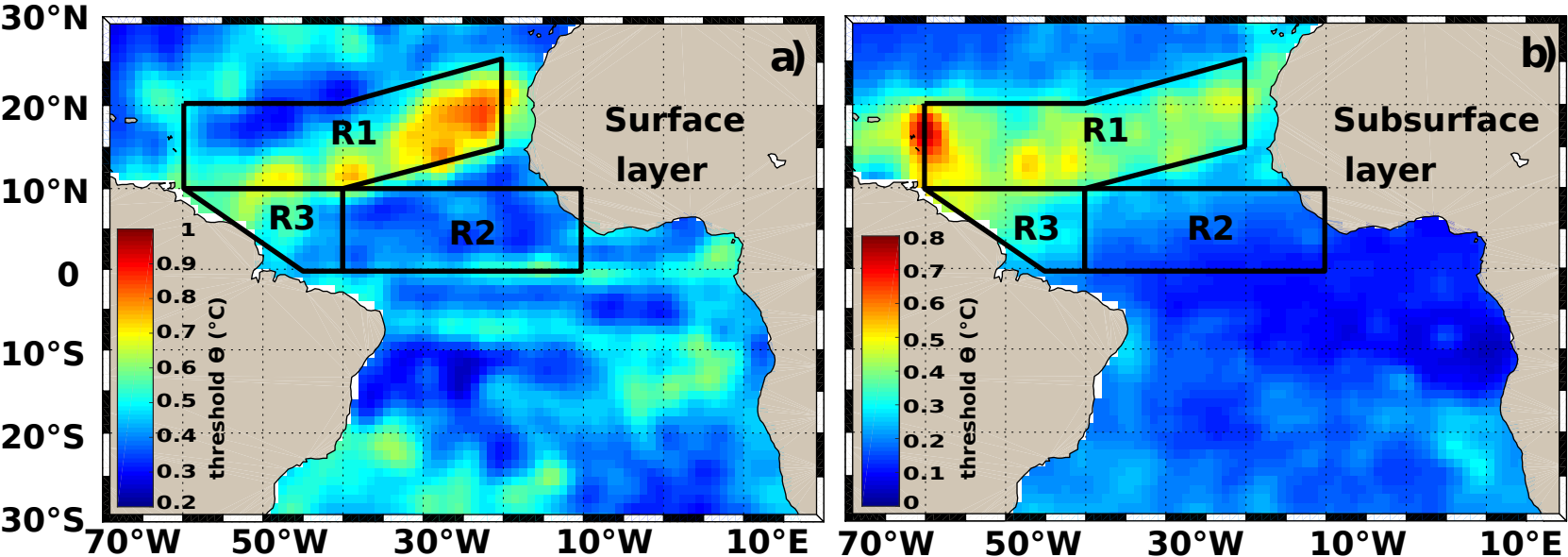
a)
b)
R1
R2
R3
Surface layer
Subsurface layer
threshold θ (°C)
1
0.9
0.8
0.7
0.6
0.5
0.4
0.3
0.2
0.8
0.7
0.6
0.5
0.4
0.3
0.2
0.1
0
30°N
20°N
10°N
0
10°S
20°S
30°S
70°W
50°W
30°W
10°W
10°E

Figure4.

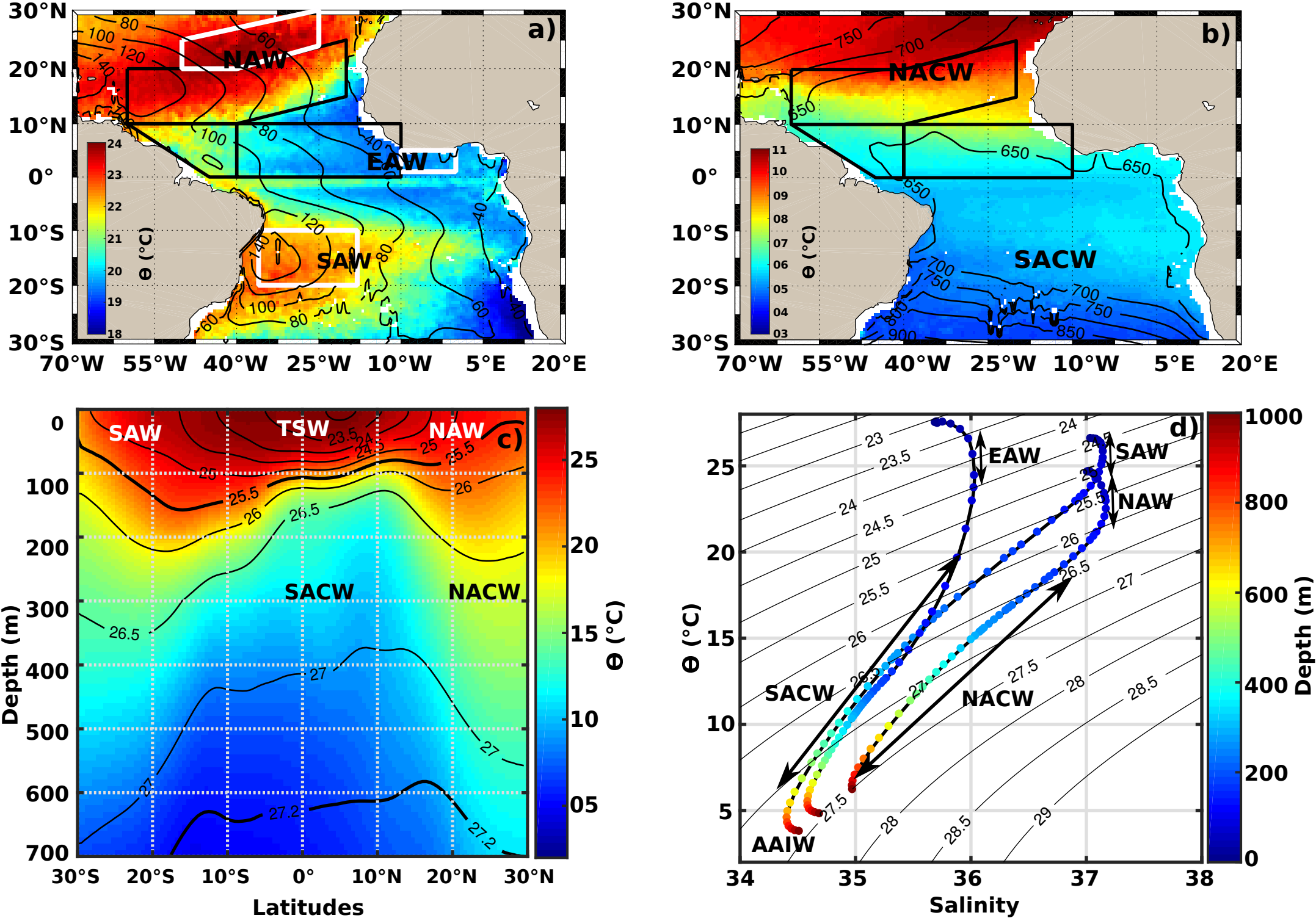
a)
NAW
EAW
SAW
θ (°C)
30°N
20°N
10°N
0°
10°S
20°S
30°S
70°W 55°W 40°W 25°W 10°W 5°E 20°E
b)
NACW
SACW
θ (°C)
c)
SAW
TSW
NAW
SACW
NACW
Depth (m)
Latitudes
30°S 20°S 10°S 0° 10°N 20°N 30°N
d)
EAW
SAW
NAW
SACW
NACW
AAIW
θ (°C)
Salinity
Depth (m)

Figure5.

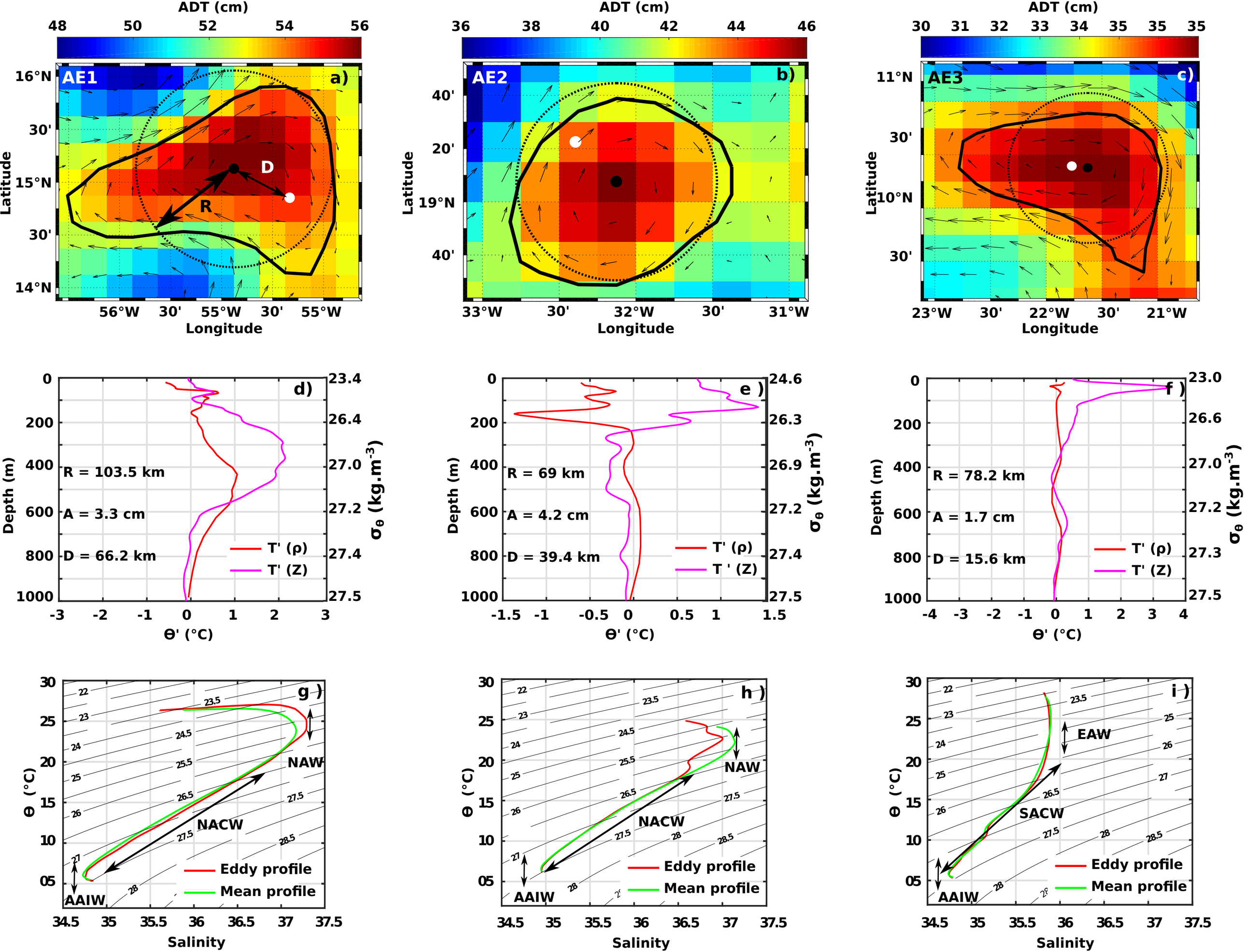
ADT (cm)
AE1
a)
D
R
Latitude
Longitude
AE2
b)
AE3
c)
d)
R = 103.5 km
A = 3.3 cm
D = 66.2 km
T' (ρ)
T' (Z)
Depth (m)
Θ' (°C)
σθ (kg.m-3)
e)
R = 69 km
A = 4.2 cm
D = 39.4 km
f)
R = 78.2 km
A = 1.7 cm
D = 15.6 km
g)
h)
i)
NAW
NACW
SACW
EAW
AAIW
Eddy profile
Mean profile
Θ (°C)
Salinity

Figure6.

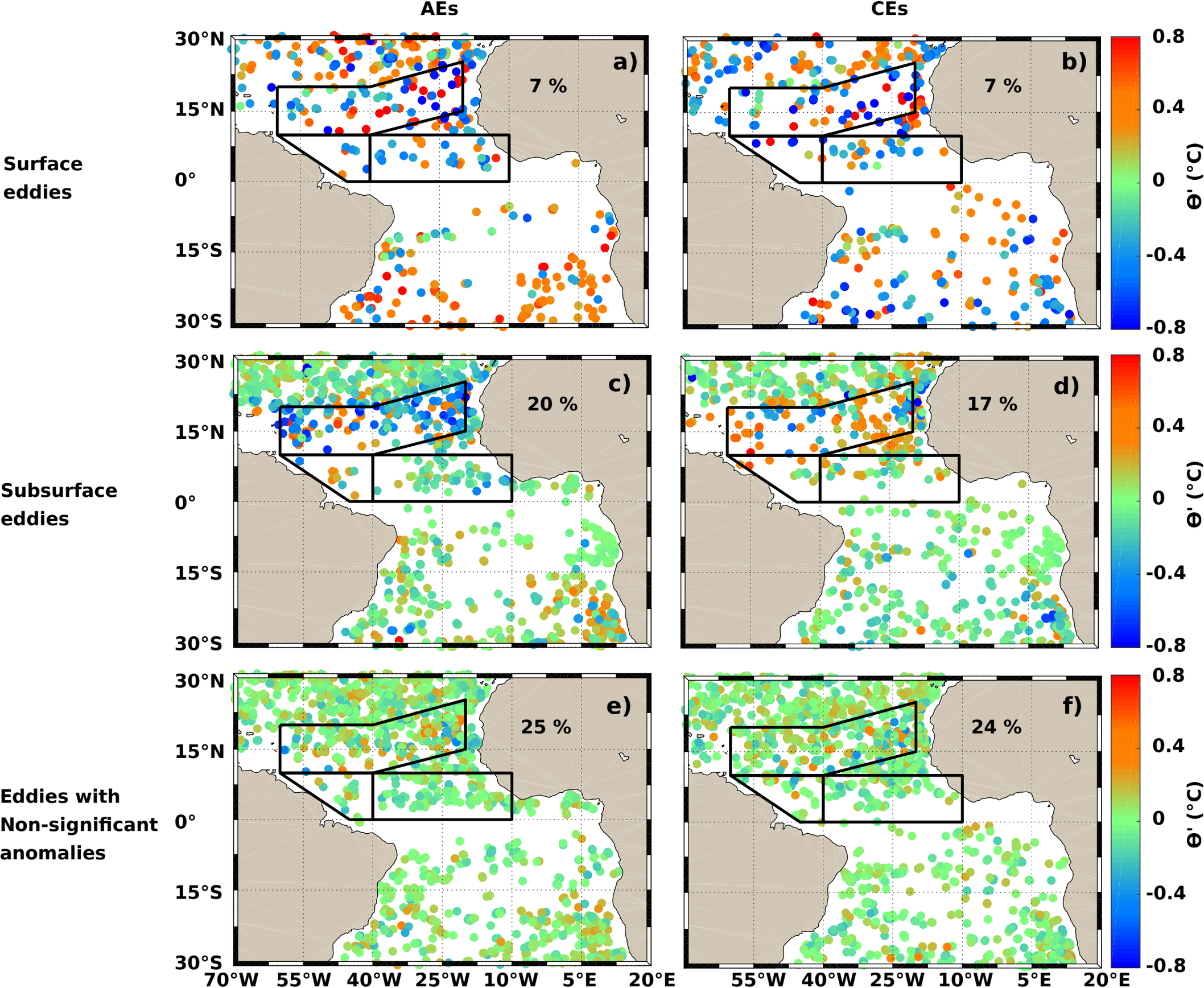
AEs
CEs
Surface eddies
Subsurface eddies
Eddies with Non-significant anomalies
a)
7 %
b)
7 %
c)
20 %
d)
17 %
e)
25 %
f)
24 %
30°N
15°N
0°
15°S
30°S
70°W
55°W
40°W
25°W
10°W
5°E
20°E
0.8
0.4
0
-0.4
-0.8
Θ' (°C)

Figure7.

R1

R2

R3

AE

CE

265

30

27

122

45

129

17

08

45

10

17

04

02

03

06

291

27

22

43

80

104

17

12

19

36

32

05

02

03

07

Density (kgm^{-3})

1022.5

1023.5

1024.5

1025.5

1026.5

1027.5

-1

-0.5

0

0.5

1

Θ' (°C)

Figure8.

Isopycnal advection

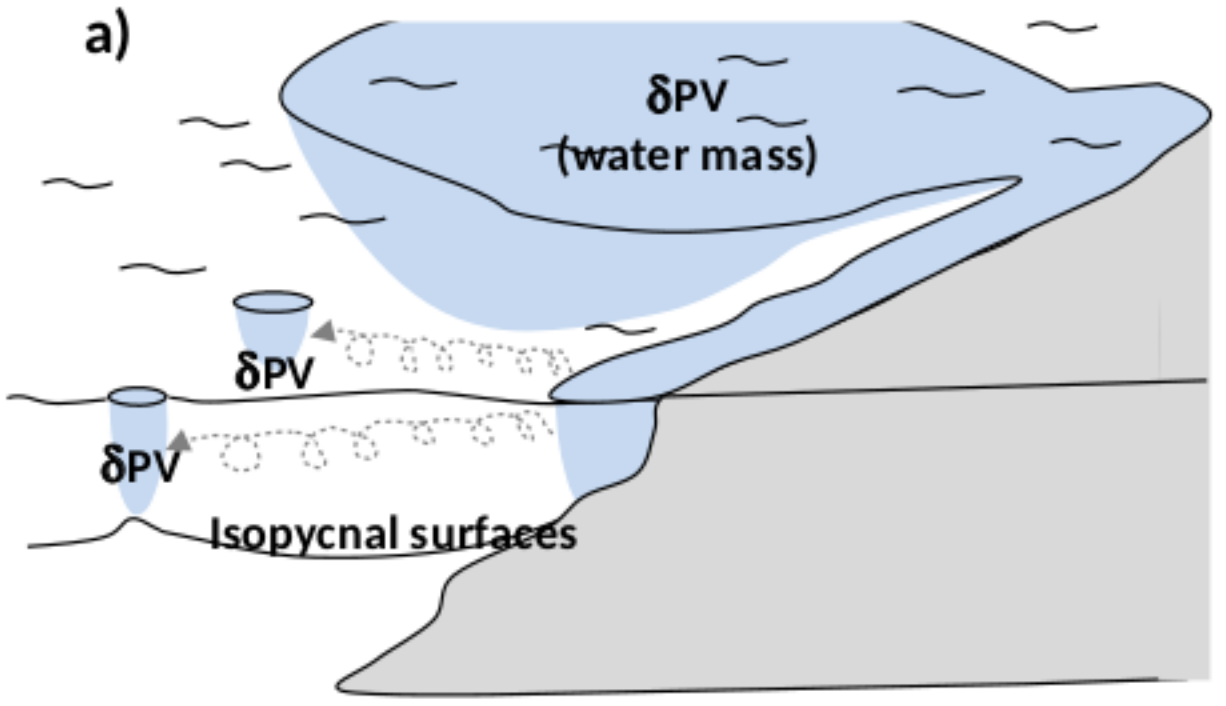

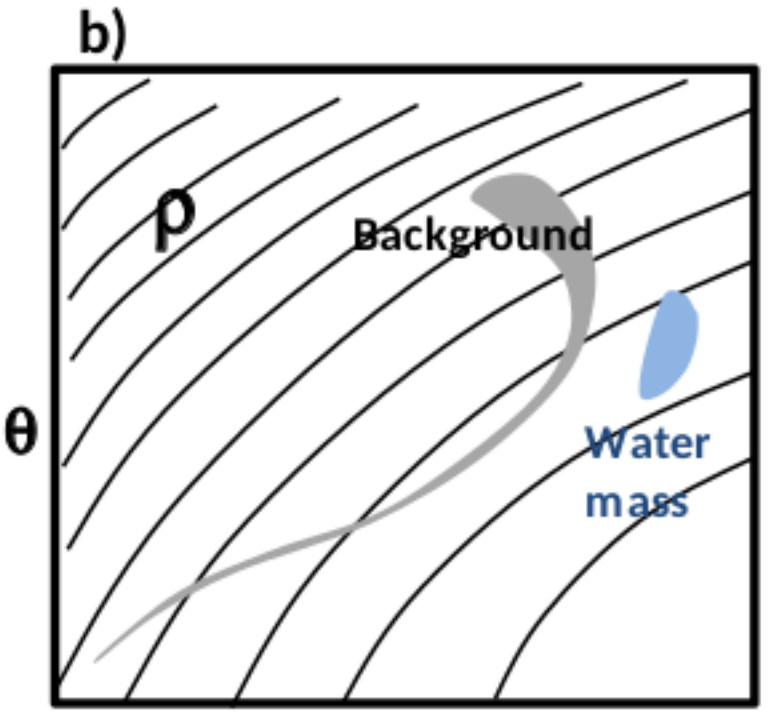

Mixing effects

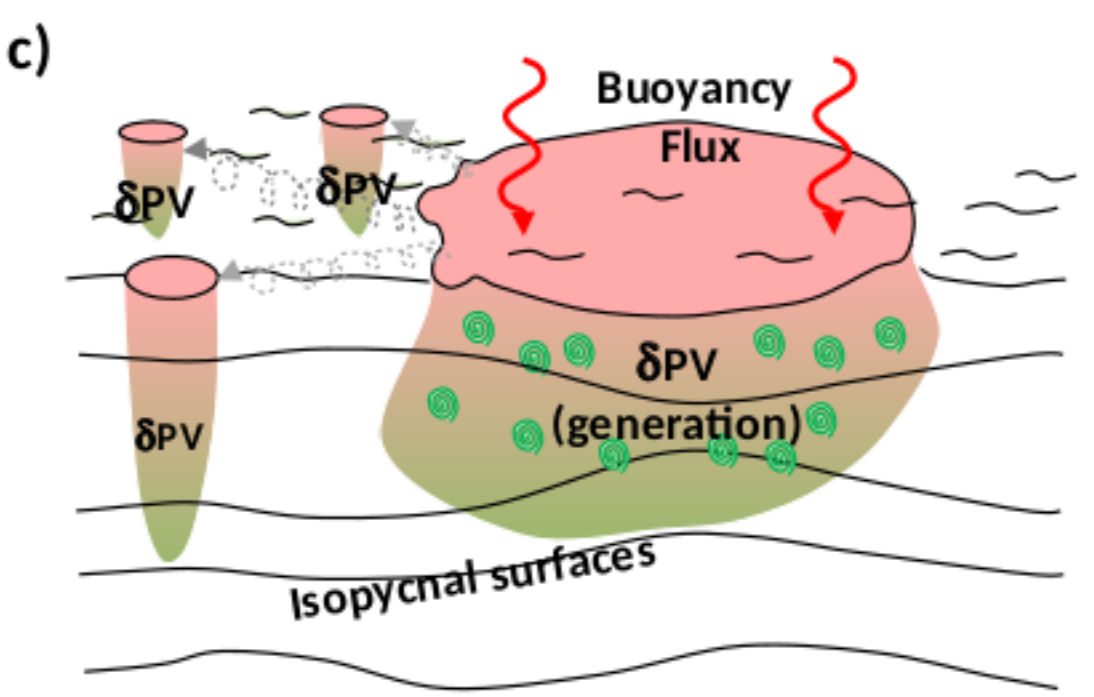

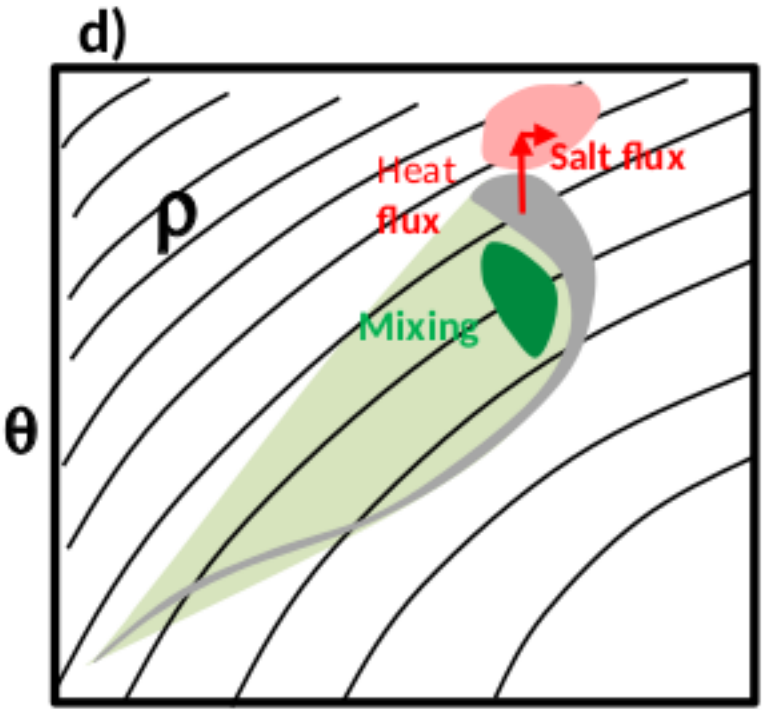

Frictional effects

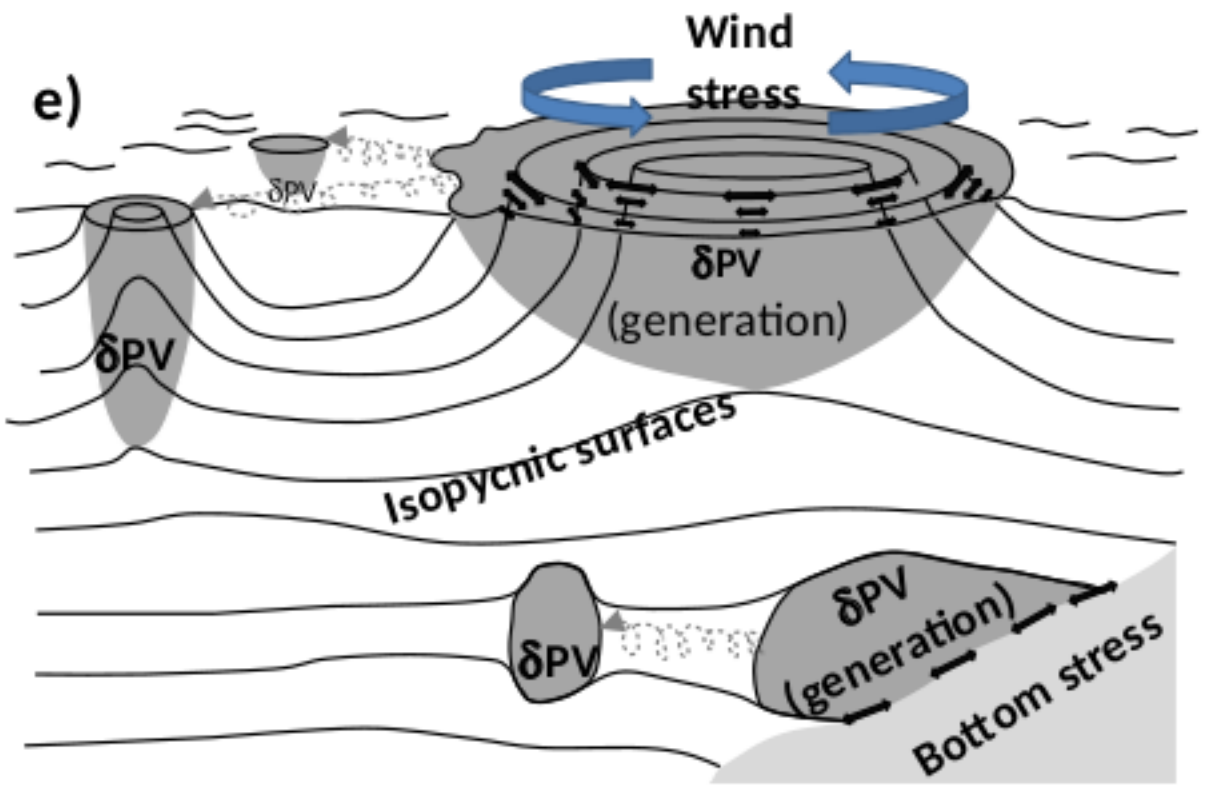

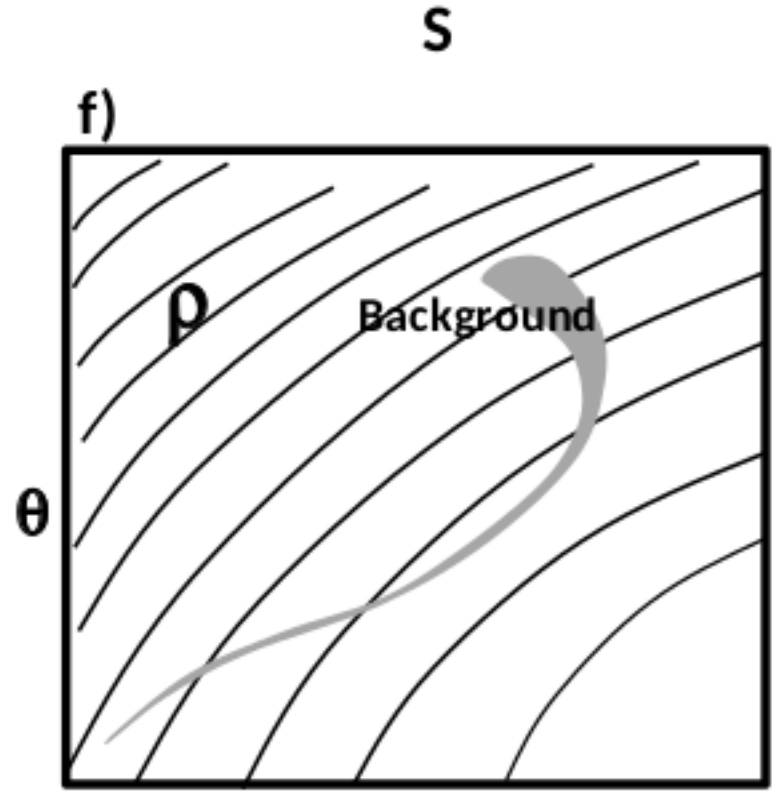

Mixing

Surface buoyancy flux

Frictional forcing

Vortex formation

Figure9.

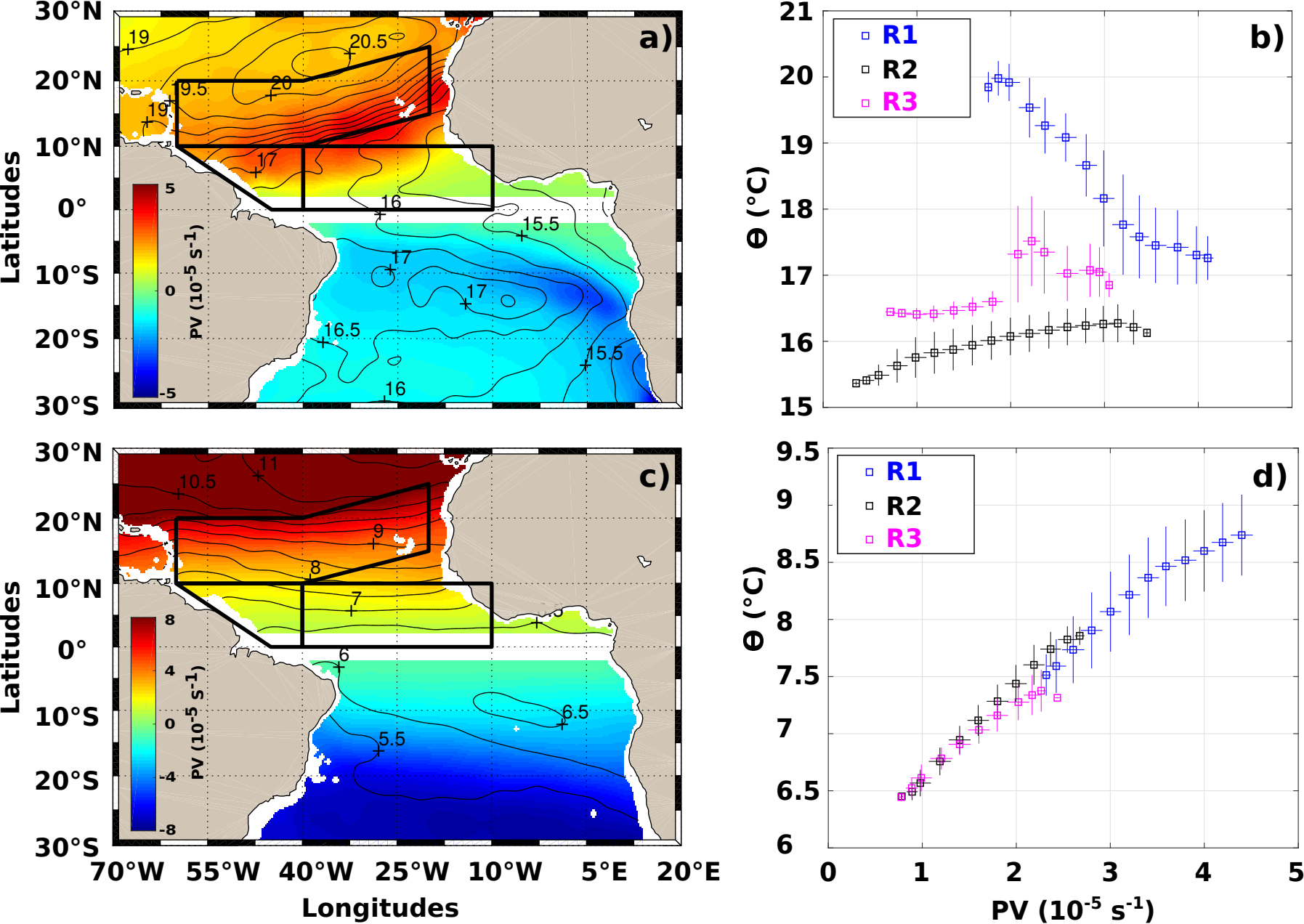
a)
b)
c)
d)
R1
R2
R3
Latitudes
Longitudes
PV (10^{-5} s^{-1})
θ (°C)
30°N
20°N
10°N
0°
10°S
20°S
30°S
70°W
55°W
40°W
25°W
10°W
5°E
20°E
0
1
2
3
4
5
6
6.5
7
7.5
8
8.5
9
9.5
10
11
12
13
14
15
16
17
18
19
20
21

Figure A1.

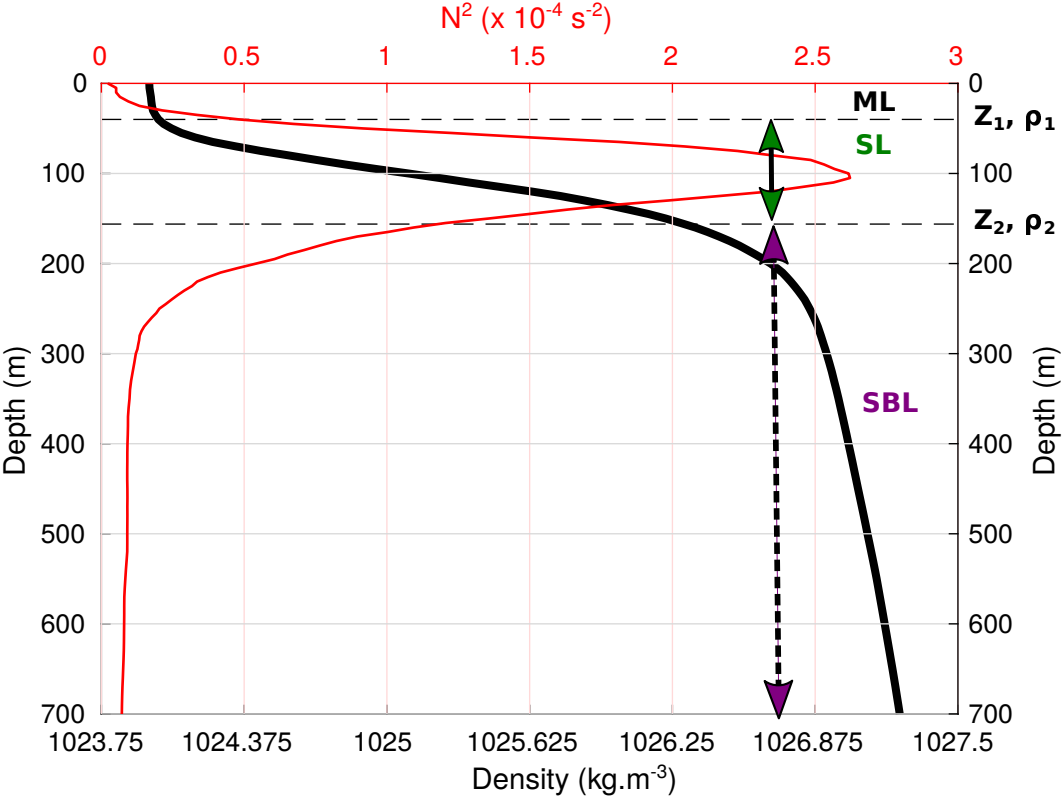
N² (x 10⁻⁴ s⁻²)
0
0.5
1
1.5
2
2.5
3
ML
SL
SBL
Z₁, ρ₁
Z₂, ρ₂
Depth (m)
0
100
200
300
400
500
600
700
1023.75
1024.375
1025
1025.625
1026.25
1026.875
1027.5
Density (kg.m⁻³)

Figure A2.

Jan
Feb
Mar
Apr
May
Jun
Jul
Aug
Sep
Oct
Nov
Dec
30°N
20°N
10°N
0°
10°S
20°S
30°S
70°W
50°W
30°W
10°W
10°E
0.2
0.4
0.6
0.8
1
Surface layer Temperature anomaly threshold (°C)

Figure A3.

Jan
Feb
Mar
Apr
May
Jun
Jul
Aug
Sep
Oct
Nov
Dec
30°N
20°N
10°N
0°
10°S
20°S
30°S
70°W
50°W
30°W
10°W
10°E
0.2
0.4
0.6
0.8
1
Suburface layer Temperature anomaly threshold (°C)

Figure A4.

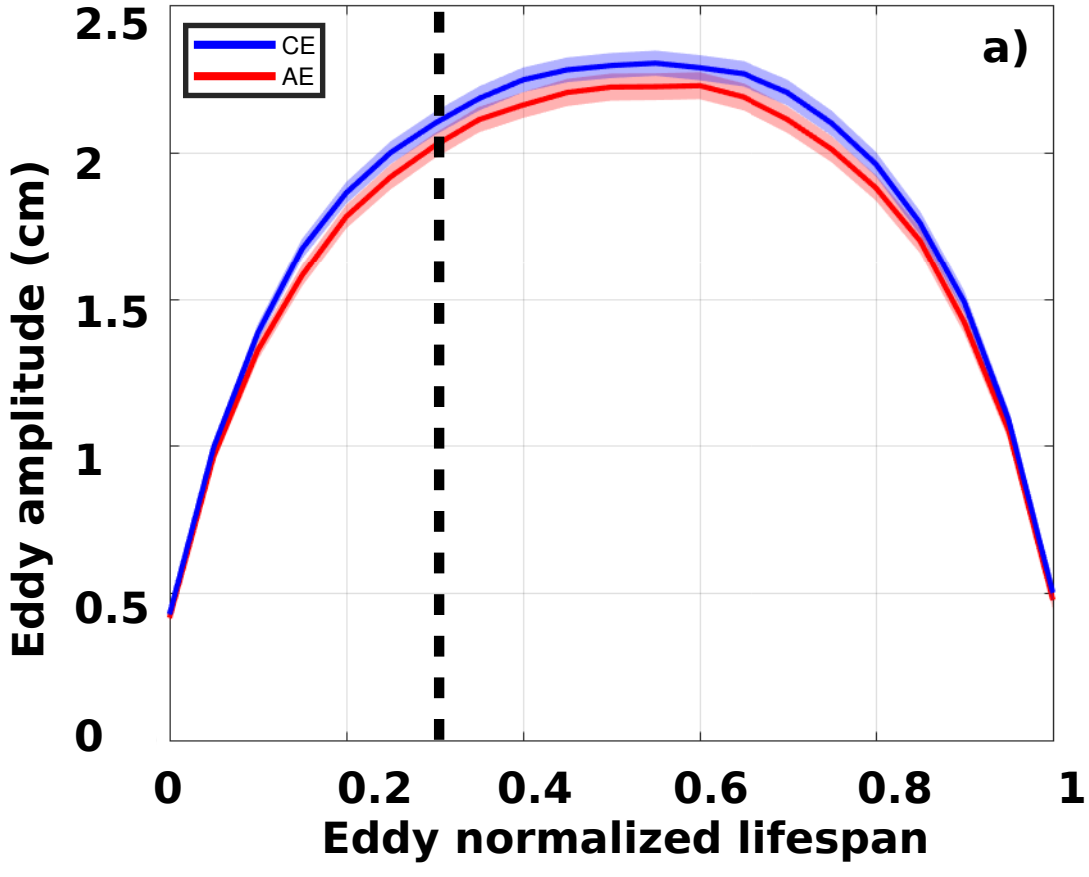
a)
CE
AE
Eddy amplitude (cm)
2.5
2
1.5
1
0.5
0
0
0.2
0.4
0.6
0.8
1
Eddy normalized lifespan

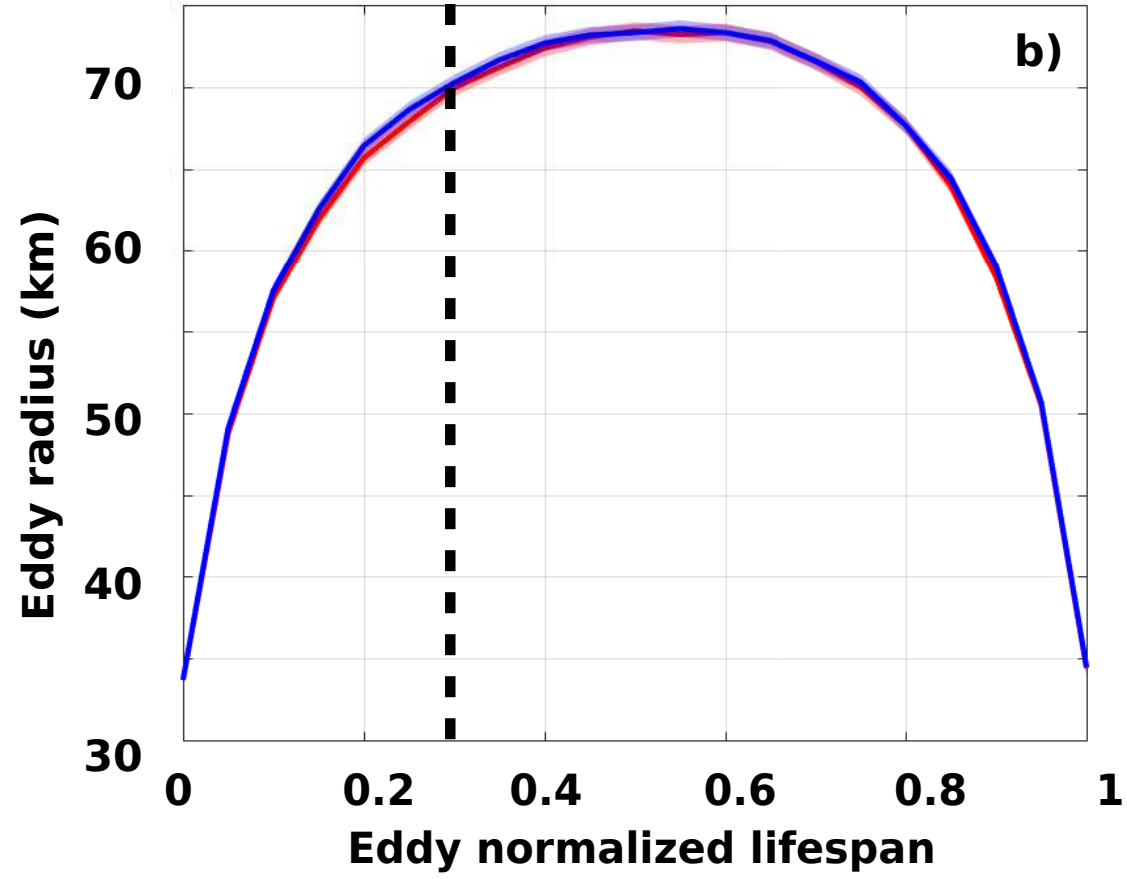
b)
Eddy radius (km)
70
60
50
40
30
0
0.2
0.4
0.6
0.8
1
Eddy normalized lifespan

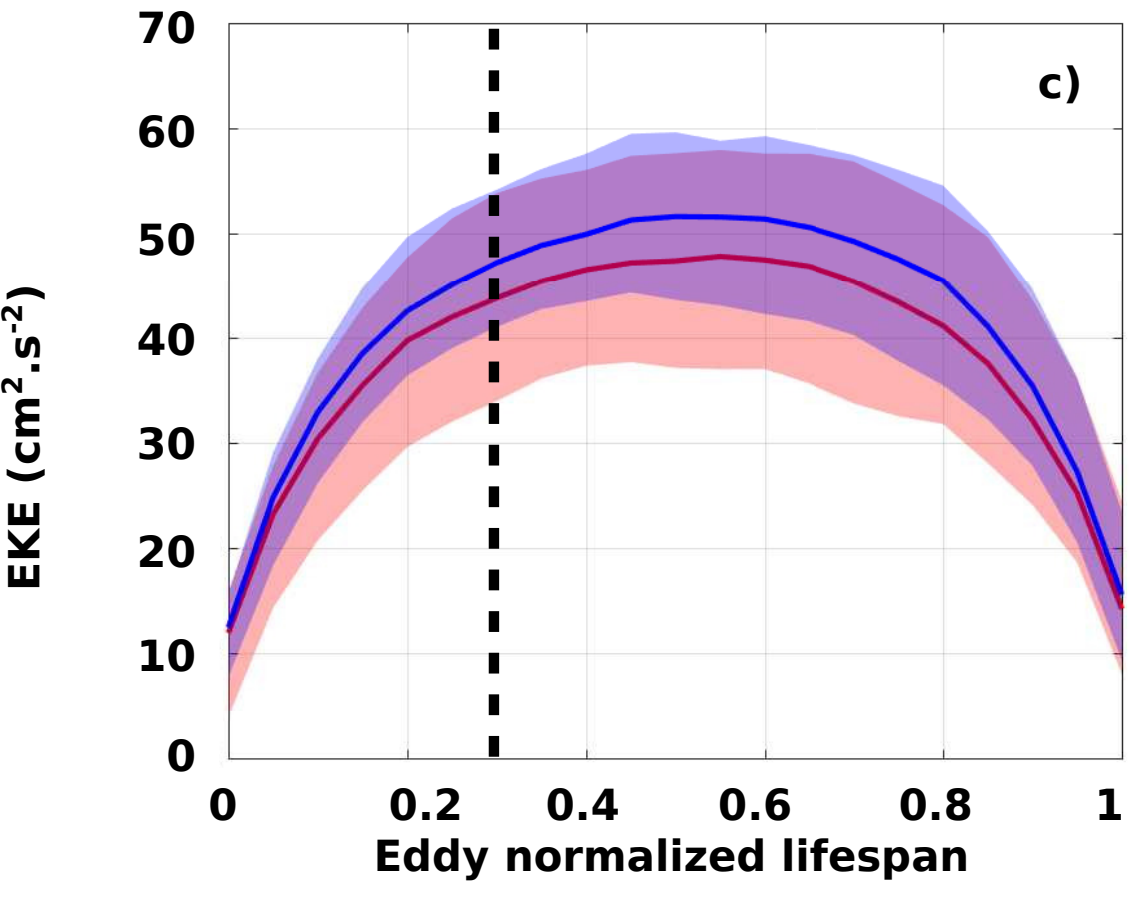
c)
EKE (cm².s⁻²)
70
60
50
40
30
20
10
0
0
0.2
0.4
0.6
0.8
1
Eddy normalized lifespan

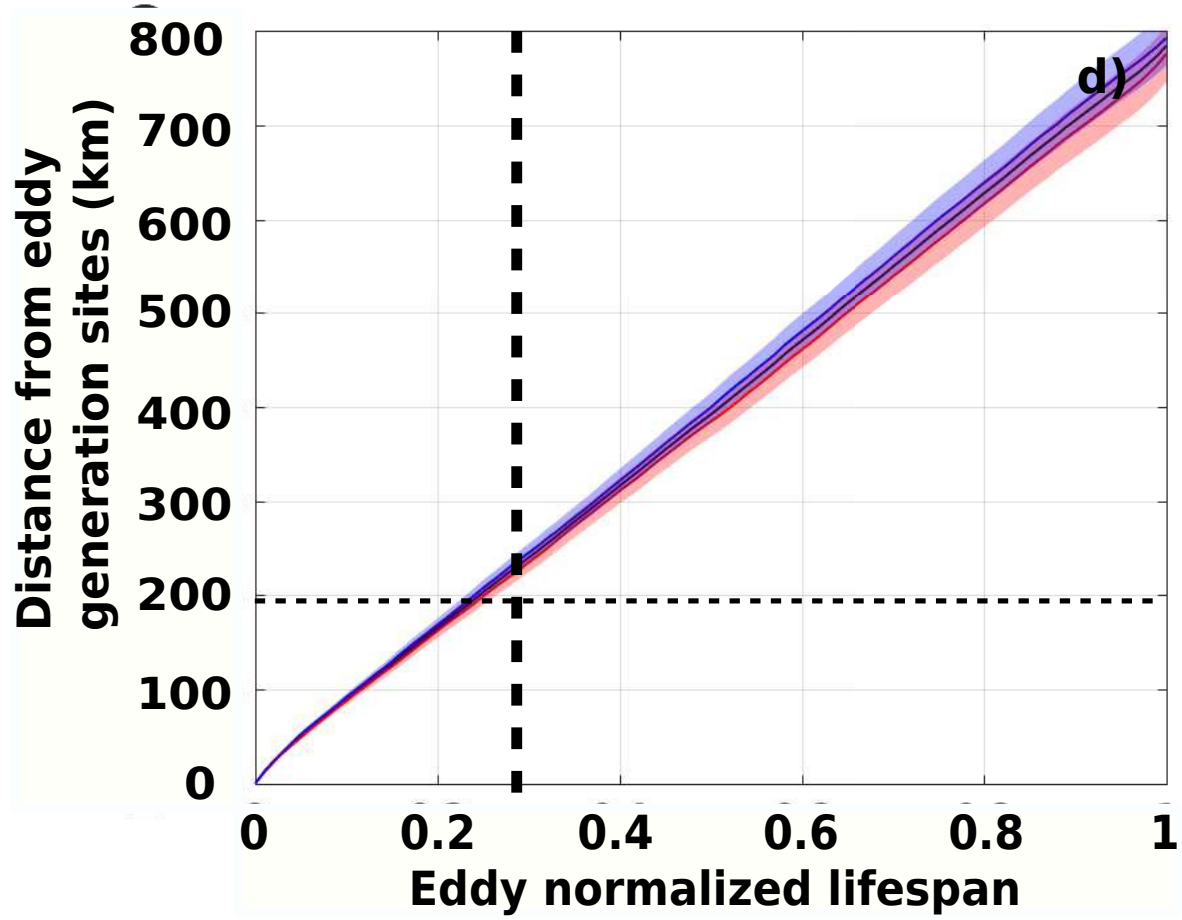
d)
Distance from eddy generation sites (km)
800
700
600
500
400
300
200
100
0
0
0.2
0.4
0.6
0.8
1
Eddy normalized lifespan